What Happens during Thermal Post-Treatment of Powder Aerosol Deposited Functional Ceramic Films? Explanations Based on an Experiment-Enhanced Literature Survey

Jörg Exner,* Tobias Nazarenus, Dominik Hanft, Jaroslaw Kita, and Ralf Moos

Powder aerosol deposition (PAD) is a unique ceramic spray coating method that produces dense and well-adhering thick-films directly at room temperature, without requiring any heating or sintering. After the successful film formation, mechanical film properties like hardness or plasma resistance are remarkably good. However, when it comes to electrical properties like permittivity or electrical conductivity, the nanocrystalline structure of PAD films combined with high internal strains deteriorates partly the characteristic properties. The electrical conductivity may already be present within the as-deposited films. However, it is mostly lowered by several orders of magnitude. Therefore, a thermal post-deposition annealing is oftentimes required. In this work, electrically conducting films produced by powder aerosol deposition are surveyed based on published data. Their microstructural and electrical behavior during the post-deposition annealing treatment is summarized and reasons for the lowered electrical conductivity are identified. Additionally, the processes taking place during annealing, which eventually allow to regain bulk-like functional properties, are examined. A universal annealing behavior is found that leads to a quantitative recommendation for the suitable film annealing temperatures to regain the electrical conductivities.

1. Introduction

In recent decades, the demand for technical ceramic components has continuously increased in a large number of applications. Conventional materials such as non-combustible, high-temperature-resistant ceramics are still of interest; however, especially new high-performance ceramics with functional material properties are on the rise.[1] These functional materials may be one of the key elements tackling climate change and environmental challenges with new clean and environmentally friendly technologies.[2] Therefore, one important direction of ongoing research are materials used

in the field of energy storage and conversion for applications in stationary or mobile battery systems, in capacitors, thermoelectric generators, and fuel cells as well as electrical generators in wind turbines.[3] In addition to fundamental materials development, processing plays an increasingly important role for exceptional mechanical and functional properties of the designed application, especially when technical ceramics with very high manufacturing temperatures are involved.[4] Besides conventional sintering of bulk ceramics,[5] ceramic coating techniques are of particular interest.[6] Almost all available ceramic film deposition processes require a high temperature heat treatment, either during film formation or afterward, to achieve a stable, well-consolidated ceramic film.[6] Necessary temperatures are typically in the range of 500–1200 °C (for vapor deposition techniques like chemical vapor deposition (CVD)[7] and physical vapor deposition (PVD)[8] as well as spray processes like plasma spray[9] or thermal spray coating[10]), therefore substantially limiting the choice of possible coating as well as substrate materials.

In contrast to these coating processes, a novel spray coating method called "aerosol deposition" overcomes many of the traditional drawbacks and owns some unique advantages. Its ceramic film deposition takes place completely at room temperature without heating neither the substrate nor the coating material, yet enables the deposition of fully dense and well-adhering films.[11,12] Furthermore, a broad range of oxide[13–15] and non-oxide[16,17] based ceramic coating materials can be processed to a large variety of substrates like metals,[18,19] ceramics,[20] glasses,[21] or even polymers.[22] Additionally, dense films are formed directly by dry spraying a sub-micrometer to micrometer-sized raw ceramic powder onto the surface to be coated without any liquids or binder involved. Only a dry carrier gas supply (i.e., air, oxygen, nitrogen, or noble gases) for the generation and acceleration of the aerosol is necessary, combined with a rough vacuum of around 1 mbar in the deposition chamber. The commonly used name "aerosol deposition method" (abbreviated as ADM or AD) was embossed by Akedo in the late 1990s;[23,24] however, several related terms such as vacuum kinetic spray (VKS),[25] vacuum cold spray (VCS),[26] nanoparticle deposition system (NPDS),[27] granule spray in vacuum (GSV),[28] and powder aerosol deposition (PAD)[29] are

Dr. J. Exner, T. Nazarenus, Dr. D. Hanft, Dr. J. Kita, Prof. R. Moos
Department of Functional Materials
University of Bayreuth
Universitätsstraße 30, 95440 Bayreuth, Germany
E-mail: Functional.Materials@Uni-Bayreuth.de

The ORCID identification number(s) for the author(s) of this article can be found under https://doi.org/10.1002/adma.201908104.

used synonymously by different research groups. To emphasize on the fact, that the deposition takes place by just spraying the dry raw ceramic powder, we prefer the term powder aerosol deposition and its abbreviation PAD, which is therefore used in this manuscript. By using PAD, we also intend to underline the difference to similar-sounding coating methods like aerosol jet printing[30] that in contrast make prominent use of liquid aerosols and require to be sintered afterward.

The claim of dense room temperature deposition of ceramic films by PAD has been proven for numerous different materials.[16,31–41] However, if functional ceramics with magnetic, dielectric, piezoelectric, or electrical conductive properties are investigated, a thermal post-deposition treatment is common,[42–50] typically referred to as annealing procedure. Akedo described the general improvement of ferroelectric functional electric properties of PAD films which takes place at significantly lower temperatures when compared to conventional thin film methods or conventional sintering.[12] Used temperatures vary depending on the functional material, but oftentimes exceed 800–1000 °C.[51–53] This of course contradicts the previously mentioned main advantage of the powder aerosol deposition method. Therefore, the following five questions arise:

1. Why is a thermal post-treatment of powder aerosol-deposited films necessary at all?
2. Why are functional properties of as-deposited PAD films different than expected?
3. What happens during annealing of PAD films?
4. Which temperatures are necessary to achieve the best functional properties?
5. Can bulk-like functional properties be regained by thermal annealing?

A deeper understanding of the processes that deteriorate the functional PAD film properties and the effect of the thermal treatment on them may allow an optimized annealing at reduced temperatures. For a better comprehension and to reduce complexity, we focus on PAD films with only one dominant functional property. We selected electrical conductive PAD films with different ionic or electronic charge carriers. These materials and the coatings produced from them may be the basis for a variety of applications, for example, in the field of energy storage and conversion. PAD films may be implemented as thin and dense solid membranes in solid oxide fuel cells (SOFC)[42,54] or all-solid-state batteries[55,56] as well as functional components in thermoelectric generators (TEG).[57,58] In addition, also various functional sensing materials utilize a temperature or gas-dependent electrical conductivity as sensor output signal. In order to answer the aforementioned questions and shed light on the effects of thermal annealing, we review the powder aerosol deposition process and summarize already published results on electrically conducting PAD films. The goal is to enable a more generalized approach to thermal annealing including an easy prediction of the lowest required post-treatment temperature.

Jörg Exner received his diploma degree in material science in 2011 and the Ph.D. degree in 2018 from the University of Bayreuth, Germany. Currently he is working as a postdoctoral researcher and project engineer at the Department of Functional Materials at the University of Bayreuth (Germany). His research is focused on aerosol deposition of functional ceramics films with semiconducting or ion conducting properties and their application in electrochemical devices.

Jaroslaw Kita received his M.Sc. degree at the Department of Electronics, Wroclaw University of Technology (Poland), in 1998. In 2003, he received the Ph.D. degree in electronics from the Department of Microsystem Electronics and Photonics at the same university. In 2004, he joined the Department of Functional Materials, University of Bayreuth (Germany), and is now a permanent member and head of technology group. His main interests are in the field of different film technologies and deposition techniques for gas sensors and ceramic microsystems.

Ralf Moos received the Diploma degree in electrical engineering in 1989 and the doctoral degree in 1995 from the University of Karlsruhe, Germany, where he conducted research on defect chemistry of titanates. He then joined Daimler Research. In 2001, he was appointed head of the Department of Functional Materials (Chair) of the University of Bayreuth. Key aspects of his research are inorganic, mainly oxide functional materials. With respect to materials, perovskites, porous framework materials, and ion conductors are in the focus. Application fields encompass sensors, catalysts, and materials for energy conversion. Special attention is given to film and layer technologies.

2. Powder Aerosol Deposition

This section summarizes the state-of-the-art of powder aerosol deposition with regard to the typical used setups and process parameters as well as to typical film morphologies. A typical PAD setup consists of three main components (**Figure 1**, left-hand side): an aerosol generation unit, a vacuum deposition chamber and a high throughput vacuum pump.
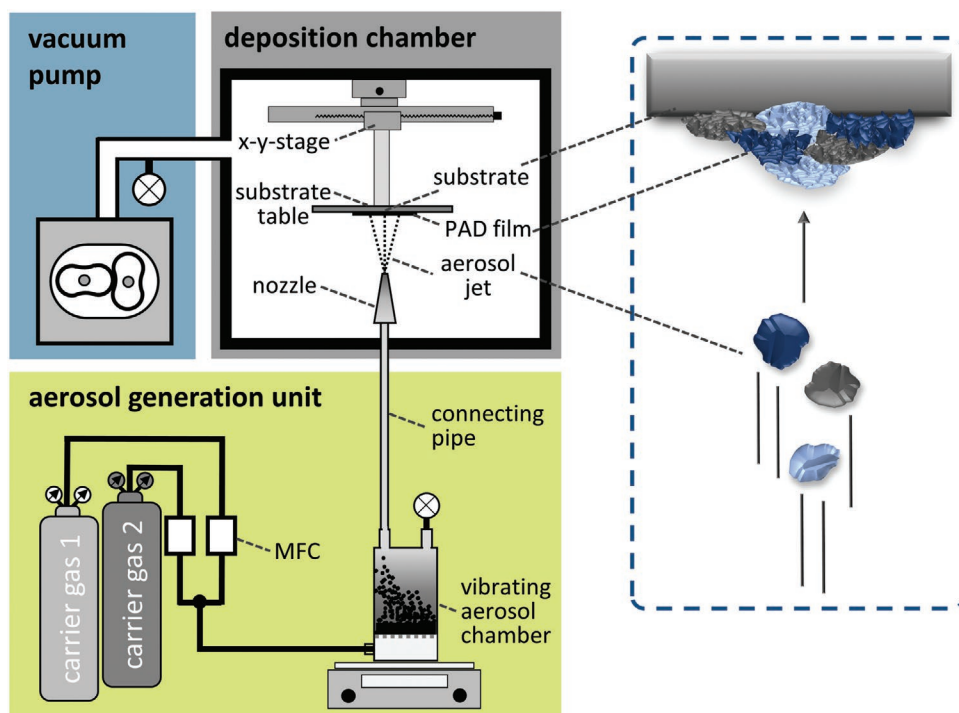
Figure 1. Schematic representation of a PAD apparatus and of the particle to film deposition mechanism. Adapted under the terms of a Creative Commons Attribution License.[11] Copyright 2015, Göller Verlag.

Aerosol generation takes place in either custom-made[59] or commercially available[60–62] aerosol generators. A continuous carrier gas flow provided by a gas supply and mass flow controllers (MFC) is necessary to form, transport and accelerate the aerosol. One or more gas species, mostly oxygen, nitrogen, air or noble gases like helium or argon are used. Custom-made aerosol generators are oftentimes intended for laboratory scale research with typical batch sizes of a few grams to several tens of grams. Powders are placed in a mechanically vibrated container wherein the aerosol is formed as a fluidized bed with the help of the carrier gas flow.[59,60] Commercially available units may use different principles, like a rotation brush to disperse a compacted powder filling as described by Hanft et al.,[60] or a fluidized bed with horizontal screens and additional bronze beads for deagglomeration as mentioned by Sarobol et al.[62] Unfortunately, in most publications only little information is given in respect to the aerosol generation and the used devices. The deposition chamber is designed to withstand a rough vacuum as well as particle contamination and is, in most cases, equipped with programmable stages (x–y or x–y–z directions) to move the substrate opposite of a fixed nozzle ejecting the aerosol. The attached vacuum pump maintains a constant vacuum at pressures between 0.2 and 20 mbar in the deposition chamber, while a continuous gas (aerosol) flow from the aerosol generation unit enters through the nozzle. Most commonly high throughput, two stage pump designs with at least one booster pump are used to reliably evacuate the steady carrier gas flow. For example, a pumping capacity of at least 600 m³ h⁻¹ is necessary to sustain an absolute pressure of 1 mbar at a gas flow rate of 10 L min⁻¹ (atmospheric pressure). An optional dust filter placed between vacuum pump

and deposition chamber protects the rotating parts of the pump from the abrasive ceramic particles.

The coating procedure itself takes place as following: The aerosol forms in the aerosol generation unit with the help of a carrier gas. It then gets transferred to the deposition chamber in hoses/pipes and subsequently gets accelerated to velocities above 150 m s⁻¹ in a nozzle,[63] driven by a pressure difference. After the aerosol ejects the nozzles orifice, the particles impact on the substrate surface and build a well-adhering film. Film growth takes place by repeatedly moving (lateral scanning) the substrate above the nozzle. The assumed and widely accepted deposition mechanism during impaction is displayed on the right-hand side of Figure 1. While different groups promote various names (AD, VCS, VKS, GSV, PAD) for the coating process itself, all methods utilize the same underlying deposition mechanism, typically referred to as room temperature impact consolidation (RTIC), that involves fracturing of impacting particles in combination with a plastic deformation of the newly formed fragments.[63] The formation of fresh, unsaturated surface while fracturing is thought to be another crucial factor,[12,64] since the new surface is highly active and promotes a better bonding. Furthermore, subsequently impacting particles additionally consolidate the already deposited film (hammering effect).[65] The superior mechanical properties of PAD films can be attributed to two independent characteristics: First, to the highly dense, well-consolidated films, as already discussed, and second, to the high adhesion of the film on the substrate caused by a seamless interface layer between both. The latter fact has not yet been fully understood. Aerosol deposited films adhere on almost any substrate material, nearly independent of the surface roughness, even if a flat surface shall be

1908104 (3 of 20)

coated. Therefore, a typical mechanical clamping of the coating material at the roughened substrate surface profile is not necessary for PAD in contrast to other spray coating processes. In cases of softer substrates like copper, aluminum, or steel, a roughening to several 100 nm of the interface layer is visible in SEM images, often described as anchoring layer. For example, Wang et al. observed an about 700 nm thick, randomly distorted anchoring layer when alumina films were applied on soft aluminum substrates, while tougher stainless steel substrates showed significantly smaller sizes around 200 nm.[66] However, for very hard alumina or sapphire substrates, Schubert et al. found no visible anchoring layer and a nearly flat film-to-substrate interface was observed.[67] New studies by Khansur et al. suppose that a change in surface chemistry and polarity as well as a physical interaction of the impacting particles with the substrate material promote a good interface and anchoring layer.[68] Naoe et al. found evidence of the formation of covalent bonds in the interface between a copper substrate and alumina particles.[69] It is furthermore expected, that the formation of the anchoring layer can be viewed independently from the processes occurring during RTIC including film build-up and densification through particle–particle interactions during impact. This also supports the idea that the deposition is divided in two subsequent stages.[11,12] The first impacting particles clean the surface and shape the anchoring layer, possibly associated with embedding a monolayer of particles. Subsequently colliding particles then participate in the film growth based on the RTIC mechanism. Exner et al. observed a reduced film stability for certain alumina films on glass, whereas the identical films on alumina substrates appeared mechanically stable.[70] For glass substrates, films oftentimes already peeled off during or subsequent to the deposition process. This indicates a lower film adhesion due to a less stable interface on glass compared to alumina. However, when suitable alumina powders with a particle size d_{50} between 1.5 and 3 µm and a compressibility index CI of 44–46% were chosen, stable films could be formed on glass too.

As a consequence of the rather complex deposition mechanism, the film morphology of PAD films significantly differs from other coating techniques like thin-film vapor deposition on the one hand and conventional thick-film processing such as thermal spray coating or screen-printing on the other. PAD films feature a nearly dense, randomly orientated nanocrystalline structure. Owing to the strong impaction during deposition, PAD films may exhibit certain distorted crystal regions up to a degree of complete amorphization.[33,66] Furthermore, there are high internal compressive strains that are present as isotropic biaxial stresses[71] and that can reach values of up to 2 GPa.[72] A more detailed description of the aerosol deposition process, its deposition mechanism, and the resulting film properties can be found in overview articles of Akedo's group from 2008[12] and more recently of our group from 2015.[11] Additionally, Schubert et al. recently published a comprehensive review article on PAD films with a focus on functional ceramics in the field of sensing and energy technology.[29]

Many new research fields for PAD films emerged in the recent years, like colored luminescent films[73] and more exotic applications like protective films of lunar regolith for the In Situ Resource Utilization (ISRU) mission from the European Space Agency (ESA)[34] or even martian regolith,[74,75] as well as ceramic brushite films for dental brackets.[76] While for these applications, the film properties are already sufficient in their as-deposited state, many other applications with electrical or magnetic functionality exhibit decreased functional properties for PAD films in the as-deposited state. This is somewhat surprising, as PAD films are already phase-pure in the desired phase, which is identical to the used ceramic powder. However, it is well known that the microstructure of ceramics significantly influences the resulting mechanical and functional characteristics,[77] especially when it comes to electrically conducting or dielectric properties. Much research on PAD films was conducted on piezoelectric lead zirconate titanate ($Pb(Zr_xTi_{1-x})O_3$, PZT)[49,78–84] and dielectric barium titanate ($BaTiO_3$).[85–89] Here, films in the untreated, as-deposited state exhibited a significantly lowered permittivity[90] and in case of piezo ceramics, also a lowered remanent polarization (P_r)[91,92] and coercive field strength (E_c).[24] Thermal post-treatment (annealing) at temperatures between 400 and 1000 °C largely increases the permittivity of PAD films.[90] This is most likely due to the pronounced grain size dependency of the permittivity[46,93,94] as well as due to effects of domains.[46,95,96] Similar effects occur for magnetic aerosol deposited nickel zinc ferrite films, where a thermal annealing increases the saturation magnetization J_s.[97] In another recent study, Khansur et al. used synchrotron X-ray diffraction on PAD-$BaTiO_3$ films and observed a reduction of intrinsic, biaxial film strains through a high temperature annealing.[98] It was also shown that a gradient in mechanical film strain in the direction of the film thickness exists. Film regions close to the substrate bear higher stresses than regions close to the film surface, likely due to a less intense hammering during particle impact. Kim et al. furthermore stated that the XRD pattern of as-deposited $BaTiO_3$ films showed a peak shift when compared with the standard phase $BaTiO_3$ cubic perovskite crystal.[99] This shift was attributed to the existing crystal lattice distortion and to residual stresses induced during PAD. A thermal treatment at 500 °C for 2 h relieved the crystal structure distortion and recovered the XRD pattern of the standard phase, simultaneously improving the dielectric properties. Kim et al. investigated the influence of a heat post-treatment on the optical properties of alumina films.[100] Here, the optical transmittance strongly increased through annealing at 400 °C in air atmosphere. As-deposited films scatter the visible light due to a vast number of crystalline defects and grain boundaries around the nanocrystallites. These alumina films exhibit high crystalline damage levels with increased strain and amorphous bands in thermodynamically unpreferred high energy states. As a consequence, the activation energy for more stable states with higher crystalline ordering is significantly reduced, and crystal growth already takes places at very low temperatures of 400 °C.

While many publications on dielectric or piezoelectric PAD films have been released, only a few focused on electrically conducting PAD films. Yamamoto et al. sprayed LATP/LCO composite electrodes for all-solid-state lithium-ion batteries where the non-annealed composite interface exhibited partially crystallized and oxygen-deficient phases.[101] Hence, the disordered and reduced interfacial hetero-structure between LCO and LATP deteriorated the electrochemical contact for lithium conduction across the interface between the two phases. In

contrast, after a film annealing procedure at moderate temperatures (way below typical sintering temperatures!), the distorted phases disappeared.

A deeper understanding of the processes during thermal annealing of PAD films could be useful for materials with thermal instabilities like $RbAg_4I_5$[55] (solid electrolyte in batteries) or Sn_4P_3[102] (lithium-ion battery anode), as well as novel hybrid halide perovskites[103] (promising material for solar cells or X-ray detectors). Already investigated and published electrically conducting PAD films from literature are surveyed in the following section and their annealing behavior is compared. Based on the gained knowledge, we intend to achieve a more holistic and detailed understanding of the influence of a thermal post-treatment on electrically conducting PAD films.

3. Behavior of PAD Films during Thermal Annealing

Already published data on electrically conductive PAD films in regard to their annealing behavior will be summarized in this section. Results are divided into the electrical as well as microstructural film properties.

3.1. Change of Electrical Conductivity

The thermal annealing behavior of eleven different PAD films with four different dominating charge transporting carriers is reviewed in regard to their electrical conductivities σ. Hence, this section is subdivided with regard to the underlying charge carrier mechanism, as outlined in **Table 1** for all used functional coating materials.

Table 1. Functional coating materials and their dominating electrical charge carriers surveyed in this section in regard to their thermal annealing behavior.

Section	Charge carriers	Electrical conducting coating material used for PAD	Refs.
3.1.1.	Oxide ions	Doped bismuth vanadate (BiCuTiVOx)	[104]
		Yttria-stabilized zirconia (YSZ)	[105]
		Gadolinium-doped ceria (GDC)	[42]
3.1.2.	Protons	Yttria-doped barium zirconate ($BaZr_{0.8}Y_{0.2}O_{3-\delta}$, BZY20)	[106]
		Yttria-doped barium cerate ($BaCe_{0.8}Y_{0.2}O_{3-\delta}$, BCY20)	[106]
		Yttria-doped barium stannate ($BaSn_{0.8}Y_{0.2}O_{3-\delta}$, BSY20)	[106]
3.1.3.	Lithium ions	LLZO ($Li_7La_3Zr_2O_{12}$)	[107,108]
		LAGP ($Li_{1.5}Al_{0.5}Ge_{1.5}(PO_4)_3$)	[109]
3.1.4.	Electrons and defect electrons	Strontium titanate ferrate ($Sr(Ti,Fe)O_3$, STF)	[110]
		Barium iron tantalate ($BaFe_{1-x}Ta_xO_{3-\delta}$, BFAT)	[111]
		Nickel manganate ($NiMn_2O_4$)	[112,113]

Unless otherwise stated, the electrical conductivity of PAD films is determined in situ upon initial heating and subsequent cooling, both steps labeled as (annealing) cycle 1. The initial heating is always conducted on as-deposited, untreated PAD films, indicating that the measuring temperature corresponds to the maximum temperature that each film under test already had reached. The subsequent cooling run of cycle 1 therefore represents the electrical conductivity after a thermal annealing at the highest measuring temperature. If σ of the identical, however previously annealed, sample was measured a second time in a consecutive run, this will be labeled as cycle 2. Temperature-dependent values of σ are plotted in an Arrhenius-like representation (logarithmic electrical conductivity log σ against reciprocal temperature $1000 \cdot T^{-1}$). Here, arrows indicate the chronological order of the measurements.

Since most studies were published on the annealing behavior of oxide ion conducting PAD films, we will report on the observed effects in detail here.

3.1.1. Oxide Ion Conducting Films

Doped Bismuth Vanadate (BiCuTiVOx): The material class of bismuth vanadate exhibits one of the highest oxide ion conductivities amongst functional ceramics at moderate temperatures between 300 and ≈ 600 °C, especially for the composition $Bi_4(Cu_{0.05}Ti_{0.05}V_{0.9})_2O_{11-\delta}$ (abbreviated as BiCuTiVOx). This compound, which is doped with 5 mol% copper and 5 mol% titanium, exhibits a high chemical stability and stabilizes the high oxide ion conductive γ-phase and thus prevents undesired transformations to lower conductive phases. Exner et al. investigated dense PAD-BiCuTiVOx films with a thickness of 5 μm on gold interdigital electrodes.[104] Oxide ion conductivities were measured in air using impedance spectroscopy. The ionic conductivity of an as-deposited BiCuTiVOx film upon heating and subsequent cooling is shown in an Arrhenius-like representation in **Figure 2**. A conventionally pressed and sintered sample with an identical composition is given as reference.[114]

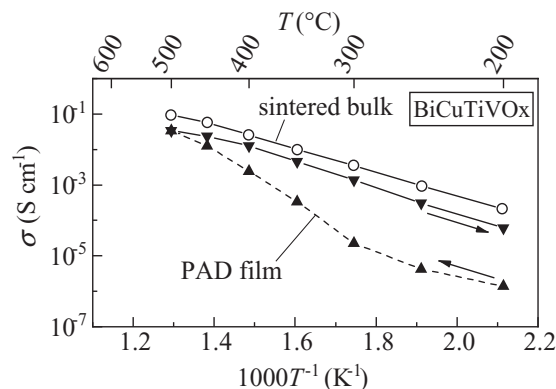The conductivity of an untreated as-deposited film during initial heating between 200 and 300 °C is by two orders of

Figure 2. Oxide ionic conductivity of a PAD-BiCuTiVOx film upon initial heating to 500 °C (▲) and subsequent cooling (▼). For comparison, values determined on sintered samples are included as well (○).[114] Arrows indicate the chronological sequence of the measurements. Adapted with permission.[104] Copyright 2014, Elsevier.

magnitude lower compared to the sintered sample. With further heating up to 500 °C, the conductivity of the film progressively approaches the σ-values of the sintered sample. At a temperature of 500 °C, the conductivity of the BiCuTiVOx film and the sintered sample almost coincide (difference less than a factor of 3). While activation energies E_a of both sample types largely differ during initial heating, the conductivities show an almost identical course upon subsequent cooling with an identical activation energy of $E_a = 0.7$ eV. The strong increase in film conductivity between 300 and 450 °C with an activation energy of 1.5 eV is particularly noticeable.

In order to investigate if the observed improvement in film conductivity is a reversible effect due to phase transformations, a consecutive second measurement cycle with the same heating and cooling rates was conducted on the identical PAD film. It is noted, that the film was cooled to room temperature before starting the second cycle. Hence, the only difference to the first measured cycle is that the PAD film was already thermally annealed at a peak temperature of 500 °C. Conductivities upon heating and cooling during cycle 2 are compared to values measured upon cooling in cycle 1 (**Figure 3**).

In the second cycle, the conductivities upon heating to 500 °C and subsequent cooling coincide well within the range of the typical measuring errors. Furthermore, conductivities also match values determined during cooling in the first cycle. Therefore, the following can be concluded: For PAD-BiCuTiVOx coatings, an irreversible change of the film occurs during the initial heating up to a temperature of 500 °C. This leads to a conductivity increase by two orders of magnitude. In this temperature region, the thermally activated oxide ion conduction is significantly increased through a superimposed annealing effect. Nevertheless, the absolute conductivity values are 2–3 times lower than those of sintered samples.

In the following, previously unpublished series of measurements, a higher peak temperature of 750 °C was chosen, aiming at a further increase in conductivity. This temperature is already very close to the optimum sintering temperature of 770–775 °C for pressed samples.[114,115] For this measurement series, again an untreated BiCuTiVOx film is used to reproduce the improvement in conductivity. **Figure 4** shows the conductivities of the BiCuTiVOx film when heated to 750 °C together with the previous measurement up to 500 °C as well as the sintered bulk sample. However, due to the geometry of the interdigital electrodes and the film, only data for temperatures up to 600 °C are shown. For higher temperatures, the measured resistance R remains almost constant at around 10 Ω regardless of the temperature. In this range, the lead resistance of the interdigital electrodes and of the sample holder wiring dominate over contributions to the PAD film.

Again, starting with untreated BiCuTiVOx films, both measurement series show an identical course of the conductivity during the initial heating in the range up to 500 °C with the already observed significant conductivity increase. With further heating up to 600 °C, the conductivity also increases due to the thermally activated oxide ionic conduction. After the peak temperature of 750 °C has been reached (not shown in the figure), conductivity values upon cooling at 600 and 550 °C perfectly match values taken at initial heating. This underlines that no further annealing effect on the electrical conductivity is present for temperatures higher than 500 °C. Independent of the applied annealing peak temperature (500 or 750 °C), low temperature conductivities upon cooling in the range of 450 °C down to 200 °C are identical.

The results promote the idea of a minimum required thermal annealing temperature $T_{annealing}$ that is necessary to irreversibly improve the ionic conductivity of the PAD-BiCuTiVOx film. Once a post deposition annealing at $T_{annealing}$ has been conducted on this PAD film, the electrical conductivities are close to bulk-like values. At this point, the question arises whether these first observations can also be transferred to different ion conducting PAD films.

Yttria-Stabilized Zirconia: Yttria-stabilized zirconia features high oxide ionic conductivities within the high temperature region between 700 and 1000 °C, combined with a high hardness, a large fracture toughness as well as a good electrochemical stability. As a consequence, it is still the state-of-the-art functional ceramic in many electrochemical devices like high temperature solid oxide fuel cells (HT-SOFC) or gas sensors (e.g., oxygen
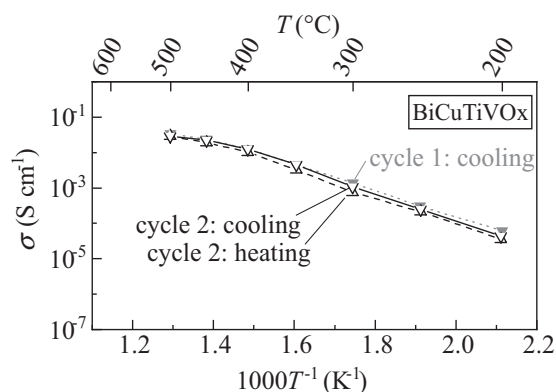
Figure 3. Oxide ionic conductivity of an PAD-BiCuTiVOx film, previously annealed at 500 °C, during cycle 2 upon heating to 500 °C (△) and subsequent cooling (▽) in comparison to values determined upon cooling during first cycle (▼). Adapted with permission.[104] Copyright 2014, Elsevier.
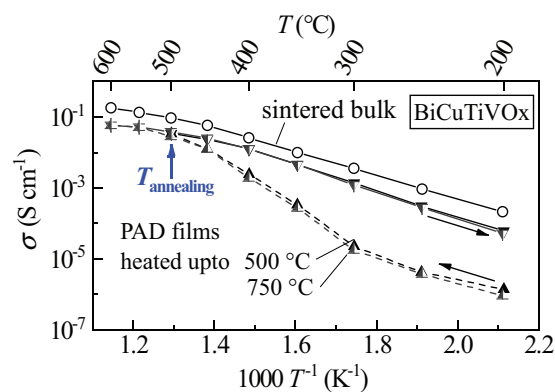
Figure 4. Oxide ionic conductivity of a PAD-BiCuTiVOx film upon initial heating to 500 °C (▲) and 750 °C (▲), respectively, followed by subsequent cooling (▼ and ▽). For comparison, values determined on sintered samples are included as well (○).[114] Arrows indicate the chronological sequence of the measurements. Adapted with permission.[104] Copyright 2014, Elsevier.

Figure 5. Oxide ionic conductivity of a PAD-8YSZ film upon initial heating to 1000 °C (▲) and subsequent cooling (▼). For comparison, values determined on sintered samples are included as well (○).[116] Arrows indicate the chronological sequence of the measurements. Adapted with permission.[105] Copyright 2019, Springer Nature.
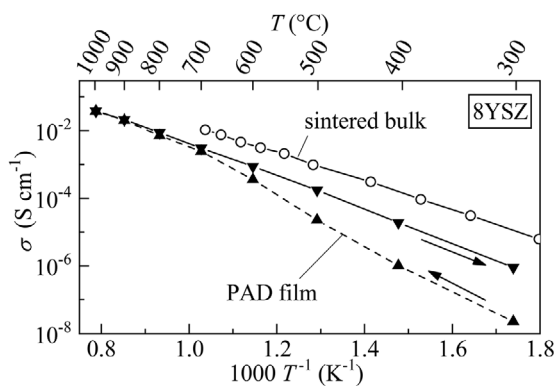
sensing lambda probe or NO_x sensors used for internal combustion engines). Thin films of yttria-stabilized zirconia (YSZ) are of particular interest to further miniaturize the devices or to enhance their performance (e.g., lower the internal membrane resistance by reducing the membrane thickness). Exner et al. manufactured dense 8YSZ (8 mol% Y_2O_3 stabilized ZrO_2) films by powder aerosol deposition and investigated their electrical properties in respect to the thermal annealing as well as to anisotropy.[105] The same setup was used as described above, however now at higher temperatures, that is, between 300 and 1000 °C. In-plane conductivities were determined using PAD-8YSZ films on platinum interdigital electrodes while through-plane values were measured using conventional parallel-plate electrodes. A slight anisotropy of the electrical conductivity was observed, possibly caused by a pan-cake-like film morphology and an increased contribution of grain boundaries due to the large number of present nanocrystallites. Therefore, through-plane conductivities including grain and grain boundary contributions are by a factor of 3 smaller than in-plane conductivities. **Figure 5** shows the behavior during initial heating using a 2.5 μm thick 8YSZ film on interdigital electrodes.

At 300 °C, the conductivity $\sigma = 2.2 \cdot 10^{-8}$ S cm^{-1} of the untreated PAD-8YSZ film is ≈40 times lower compared to the same film annealed at 1000 °C with $\sigma = 8.9 \cdot 10^{-7}$ S cm^{-1}. As

the temperature increases, the conductivities converge, until at 900 °C their difference is eventually smaller than 10%. Thus, also oxide ion conducting 8YSZ shows a high influence of the film post-treatment on its conductivity, as already observed for bismuth vanadate PAD films. In contrast, significantly higher heat treatment temperatures of 900–1000 °C are required in order to restore the bulk conductivity. For 8YSZ, the derived necessary annealing temperature $T_{annealing}$ of 900 °C is 400 °C higher than for bismuth vanadate. The conductivity of the 8YSZ film tempered at 1000 °C is slightly below the values determined on sintered samples.[116] At 700 °C, the conductivity of the PAD film σ_{PAD}, is again by a factor of 3 below that of a classical bulk-type ceramic (σ_{bulk}). One may explain this small, yet still remaining difference in the electrical conductivity between bulk and PAD film as a result of the nanocrystalline film morphology and the therefore increased contribution of grain interfaces to the total conductivity. The activation energy $E_a = 0.97$ eV of the annealed PAD-8YSZ films (during cooling) is slightly higher than the bulk value of $E_a = 0.91$ eV of the sintered samples, but corresponds very well with the activation energy $E_a = 0.98$ eV of 8YSZ thin films applied by an electrostatic spray coating.[116]

Gadolinium-Doped Ceria: Depending on the surrounding gas atmosphere, gadolinium-doped ceria ($Gd_xCe_{1-x}O_2$, abbreviated as GDC) is either an oxide ion conductor[117] or a mixed ionic-electronic conductor.[118] Mixed ionic-electronic conduction (MIEC) occurs preferably at low oxygen partial pressures and high temperatures, because both, electrons as well as oxide ions are transported. At high oxygen partial pressures, typically as present in air, GDC acts predominantly as an oxide ion conductor. GDC10 (ceria doped with 10 mol% gadolinium) films with a thickness of 1.2 μm were prepared by powder aerosol deposition.[42] Films on platinum interdigital electrodes were characterized in an alumina furnace in air by impedance spectroscopy between 400 and 1000 °C upon heating and cooling (**Figure 6**).

In the first cycle with an untreated GDC10 film (Figure 6a), the conductivity σ during heating and cooling differs slightly. At 300 °C, σ of the untreated film is by a factor of 3 smaller than after annealing at 1000 °C. In the range 300–700 °C, the difference between both measuring directions diminishes with increasing temperature. At 800 °C and higher, the conductivities are identical. The influence of annealing on the conductivity is therefore very small in case of PAD-GDC films. In a consecutive second cycle, the curves for heating and cooling
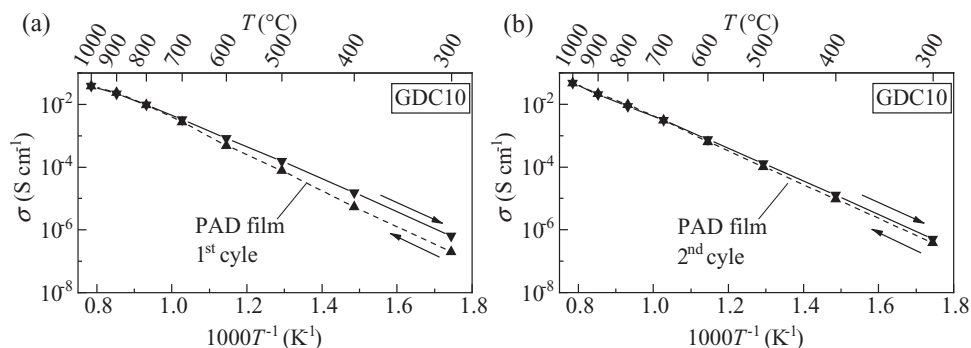

Figure 6. Oxide ionic conductivity of a PAD-GDC film upon initial heating to 1000 °C (▲) and subsequent cooling (▼) during a) first cycle and b) consecutive second cycle. Arrows indicate the chronological sequence of the measurements. Adapted under the terms of a Creative Commons Attribution License.[105] Copyright 2019, MDPI.

**ADVANCED
SCIENCE NEWS**

www.advancedsciencenews.com

**ADVANCED
MATERIALS**

www.advmat.de

are identical over the entire measured temperature range. This again indicates that the annealing is already completed during the first thermal treatment up to 1000 °C and that a further heat treatment at the same temperature does not improve the conductivity. The activation energies during cooling are almost identical with E_a = 1.00 and 1.02 eV within the first and second cycle, respectively. Measured E_a values coincide well with values determined on polycrystalline GDC films (E_a = 0.99 eV).[119] For sintered samples, Lübke and Wiemhöfer were able to distinguish between the activation energies of the grain boundaries and the grains.[120] While grain boundary conductivity (σ_{gb}) exhibits a larger activation energy of $E_{a,gb}$ = 1.3 eV, values for the grain conductivity (σ_g) are lower with $E_{a,g}$ = 0.81 eV. Since in PAD-films both components equally contribute to the total conductivity and are typically not distinguishable due to the nanocrystalline film structure, E_a of GDC10 film is in between values of grain and grain boundary.

3.1.2. Proton Conducting Films

In a recently published work, also proton conducting thick-films of three different barium-based perovskites (ABO$_3$ structure) were produced by PAD and were examined with respect to their electrical properties as well as to their thermal annealing behavior.[106] The investigated compounds originated from the material classes of barium zirconate (BaZrO$_3$), barium stannate (BaSnO$_3$), and barium cerate (BaCeO$_3$), and all were substituted by 20 mol% yttrium to replace the metallic b-site cation. The results are summarized within this subsection. These ceramic compounds feature a high chemical and thermal stability in conjunction with high protonic conductivities up to 10^{-2} S cm^{-1} at 600 °C.[121] While such properties make them promising candidates for potential use in SOFCs, a major drawback of the material classes previously existed in form of very high sintering temperatures up to 1800 °C, especially for yttria-doped barium zirconate.[122] However, dense and gas-tight membranes with thicknesses between 5 and 10 μm could be easily produced by powder aerosol deposition.

Yttria-Doped Barium Zirconate: Powders in the composition BaZr$_{0.8}$Y$_{0.2}$O$_{3-\delta}$ (abbreviated as BZY20) were sprayed on platinum interdigital electrodes. A 5 μm thick film was examined in air between 400 and 1000 °C upon heating and cooling (**Figure 7**).

At the first measured temperature of 400 °C, the conductivity of BZY20 is initially extremely low with $\sigma < 3\cdot10^{-8}$ S cm^{-1}. However, as already observed for oxide ion conducting films, the conductivity increases during initial heating up to 800 °C with a very high activation energy E_a of 1.73 eV. With further heating to 1000 °C, the slope decreases progressively. At the highest measured temperature of 1000 °C, the conductivity σ = 1.4$\cdot10^{-2}$ S cm^{-1} of the film is close to the sintered bulk sample (σ = 3.6$\cdot10^{-2}$ S cm^{-1}). During cooling, the activation energy of 0.88 eV for the PAD-BZY20 film eventually correspond well with the values of 0.93 eV given by Kreuer et al. for an identical composition.[123] After a thermal annealing procedure at 1000 °C, a significantly higher conductivity of 1.7$\cdot10^{-5}$ S cm^{-1} was measured when returning to the lowest measuring temperature of 400 °C. This corresponds to a
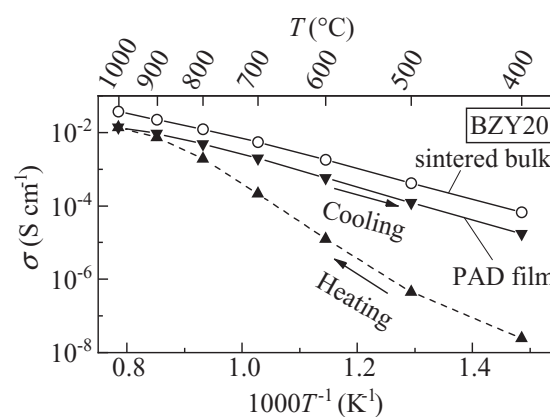

Figure 7. Protonic conductivity of a PAD-BZY20 film upon initial heating to 1000 °C (▲) and subsequent cooling (▼). A sintered bulk sample, produced from the identical powder, is included as a reference (○).[106] Arrows indicate the chronological sequence of the measurements. Adapted with permission.[106] Copyright 2020, Elsevier.

massive enhancement of the protonic conductivity by a factor of 700 compared to the untreated, as-deposited film. Beyond that, an even larger increase through thermal annealing may be possible, which is given by two indicators. On the one one hand, at the second highest measuring temperature of 900 °C, a difference in conductivity before and after annealing can still be measured, in contrast to bismuth vanadate (Figure 2) and 8YSZ (Figure 5) films. On the other hand, even after annealing at 1000 °C, this film still exhibited a microstrain (discussed in detail in Section 3.2). Thus, a further increase of the conductivity by even higher annealing temperatures would be plausible. A necessary annealing temperature $T_{annealing}$ of 900–1000 °C sounds unusually high and seems to undermine the advantage of powder aerosol deposition to fabricate dense ceramic films at room temperature. However, when compared to typical sintering temperatures for barium zirconates of 1600–1750 °C,[124,125] $T_{annealing}$ of PAD films is still in a moderate temperature range. Additionally, the dense and gas-tight microstructure of PAD films is also highly beneficially, especially since no binders were used for manufacturing.

Yttria-Doped Barium Cerate: A 9 μm thick PAD film of BaCe$_{0.8}$Y$_{0.2}$O$_{3-\delta}$ (abbreviated as BCY20) on platinum interdigital electrodes was examined by impedance spectroscopy (air atmosphere, temperatures between 300 and 900 °C upon heating and cooling). Protonic conductivities of BCY20 are shown in **Figure 8**.

The conductivity during heating increases from 5.0$\cdot10^{-6}$ S cm^{-1} at 400 °C to 8.7$\cdot10^{-3}$ S cm^{-1} at 900 °C with an average activation energy E_a of 0.99 eV. After annealing at 900 °C, the activation energy E_a = 0.54 eV is lower, but slightly higher than for sintered BCY20 samples with an E_a of 0.45 eV. At 400 °C, the conductivity of 1.9$\cdot10^{-4}$ S cm^{-1} after the annealing procedure is about 38 times higher than for the untreated film, but by a factor of 3 below the sintered sample.[126] If the derived conductivities at 300 °C instead of 400 °C are compared, an even higher improvement factor of 65 exists. It is again possible that a higher annealing temperature could further increase the electrical conductivity, since at the second highest measured temperature of 800 °C, there is still a difference of 40% between
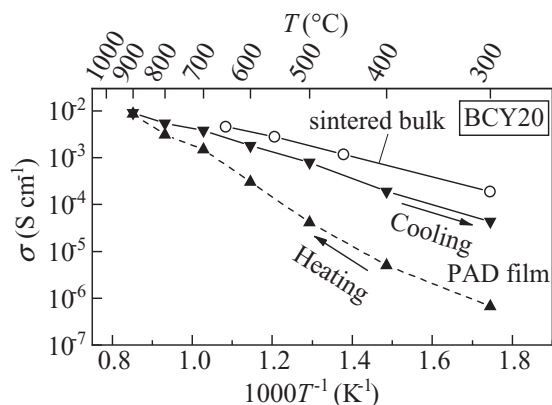
1908104 (8 of 20)

ADVANCED
SCIENCE NEWS
www.advancedsciencenews.com

ADVANCED
MATERIALS
www.advmat.de

Figure 8. Protonic conductivity of a PAD-BCY20 film upon initial heating to 900 °C (▲) and subsequent cooling (▼). A sintered BCY20 bulk sample is included as a reference (○).[126] Arrows indicate the chronological sequence of the measurements. Adapted with permission.[106] Copyright 2020, Elsevier.

the heating and the cooling direction. Therefore, the optimal annealing temperature $T_{annealing}$ is presumably above 900 °C. However, the course of heating and cooling runs also suggests, that $T_{annealing}$ may not exceed 1000 °C.

Yttria-Doped Barium Stannate: A 5 μm thick film of $BaSn_{0.8}Y_{0.2}O_{3-\delta}$ (abbreviated as BSY20) was investigated with a similar procedure as the BZY20 film. The resulting conductivities are displayed in **Figure 9**.

The conductivity of the BSY20 film at 400 °C is $2.2 \cdot 10^{-6}$ S cm^{-1} during the initial heating and thus again below a sintered bulk sample,[127] but only by 1.5 orders of magnitude. During heating, the conductivity of the BCY20 film increases to $4.5 \cdot 10^{-3}$ S cm^{-1} at 1000 °C with a high activation energy of $E_a = 0.98$ eV (sintered sample: $E_a = 0.60$ eV). During subsequent cooling, the film shows the bulk-like behavior with an identical activation energy of 0.60 eV. In addition, the total conductivity of both samples closely corresponds with only a small difference by a factor of two. Therefore, the thermal annealing behavior of the powder aerosol deposited BSY20 film
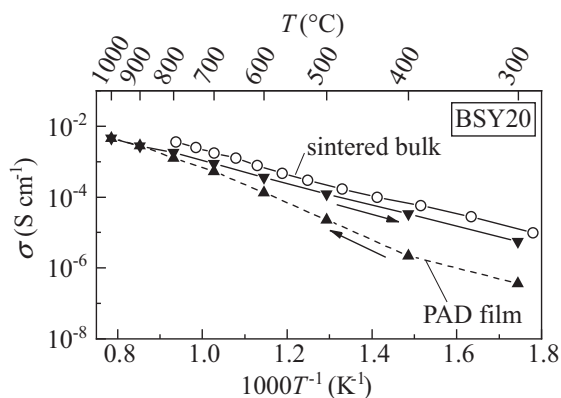
generally follows that of the BZY20 and BCY20 films. However, it appears that a lower annealing temperature may be sufficient for BSY20. At $T_{annealing}$ = 900 °C, the conductivities for heating and cooling are the same, which means that the annealing process is completed.

The following general behavior can be observed for all measured functional perovskite films produced by powder aerosol deposition: The electrical conductivity of the untreated films after powder aerosol deposition is significantly reduced, typically by one to three orders of magnitude. Again, through a moderate heat treatment of the films at 900–1000 °C, the electrical conductivities are permanently increased in all cases and almost reach the bulk values.

3.1.3. Lithium-Ion Conducting Films

Lithium-ion batteries need a highly lithium conducting electrolyte that transfers Li$^+$ between the anode and the cathode while simultaneously avoiding a direct contact of both electrodes (short-circuit). Conventional batteries need two components to achieve these requirements: A porous separator and a liquid or gel-like electrolyte. Since mostly polymer materials are used, this system still may suffer from thermal runaways. All-solid-state batteries are believed to offer higher safety levels, especially if high-temperature tolerant functional ceramics are used, as well as increased specific cell capacities. This is achieved by a thin lithium-ion conducting ceramic membrane. At the same time, it ensures the separation of the cathode and the anode. Two functional ceramics, $Li_7La_3Zr_2O_{12}$ and $Li_{1.5}Al_{0.5}Ge_{1.5}(PO_4)_3$ (abbreviated as LLZO and LAGP, respectively), feature high ionic conductivities above 10^{-4} S cm^{-1} and are currently investigated as solid electrolyte membrane in all-solid-state batteries.

Hanft et al. produced films of Al-doped and Ta-substituted cubic LLZO ($Al_yLi_{7-3y-z}La_3Zr_{2-z}Ta_zO_{12}$) by PAD and examined their conductivity σ_{RT} at room temperature utilizing electrochemical impedance spectroscopy.[108] As-deposited PAD-LLZO films showed very low conductivities of less than $3 \cdot 10^{-7}$ S cm^{-1}, almost three orders of magnitude lower than it can be found in literature (**Figure 10**).
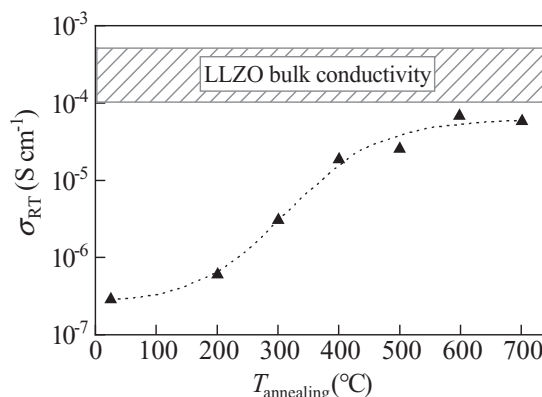

Figure 9. Protonic conductivity of a PAD-BSY20 film upon initial heating to 1000 °C (▲) and subsequent cooling (▼). A sintered BSY20 bulk sample is given as reference (○).[127] Arrows indicate the chronological sequence of the measurements. Adapted with permission.[106] Copyright 2020, Elsevier.

Figure 10. Lithium-ion conductivity at room temperature, σ_{RT}, of a PAD-LLZO film after thermal annealing at different $T_{annealing}$ (▲). The shaded region marks typical LLZO bulk conductivity values.[128–130] Adapted with permission.[108] Copyright 2017, Elsevier.

**ADVANCED
SCIENCE NEWS**

www.advancedsciencenews.com

**ADVANCED
MATERIALS**

www.advmat.de

Identical LLZO films were annealed at varying temperatures between 200 and 700 °C with heating and cooling rates of 25 K min^{-1} and a dwell time of 20 min each at the peak temperature. With increasing temperatures of the thermal post-treatment, the conductivity σ_{RT} progressively increased to $7 \cdot 10^{-5}$ S cm^{-1} after 600 °C and reached almost the reported bulk values.[128–130]

In another study by Khan et al., PAD-LAGP films were investigated.[109] A similar behavior as for LLZO was observed. Whereas as-deposited LAGP films exhibited a conductivity of less than 10^{-8} S cm^{-1}, thermal annealing at 600 and 750 °C yielded a rise in σ_{RT} to 10^{-5} and 10^{-4} S cm^{-1}, respectively. Khan et al. explained the low conductivity after PAD viewing at TEM images of the film. Here a co-existence of amorphous phases and nanocrystalline grains was visible. The increase in conductivity through thermal annealing was related to a provoked microstructural evolution with increased crystallinity.

For both investigated battery membrane materials, a moderate film annealing resulted in a large increase in the room temperature conductivity of 2.5–4 orders of magnitude. In both cases, σ_{RT} after annealing reached values around 10^{-4} S cm^{-1} which is close to the bulk conductivity.

3.1.4. Electronic Conductors

Since almost all investigated ion conducting PAD films showed a high influence of the thermal annealing on the present electrical properties, it is of large interest whether this also applies to electronically conductive (or semiconducting) materials.

Strontium Titanate Ferrate: Iron substituted strontium titanate Sr(Ti,Fe)O$_3$ is a perovskite type, semiconducting ceramic that has attracted attention due to its resistive oxygen sensing capability.[131,132] For compositions with iron contents below 50%, e.g. SrTi$_{0.65}$Fe$_{0.35}$O$_{3-\delta}$ (abbreviated as STF35), the pO_2 sensitivity has been found to be independent of temperature, and is therefore advantageous for resistive oxygen sensors. Sahner et al. produced STF35 films by powder aerosol deposition and described the simplified preparation method over conventional screen-printed and sintered films.[59] Exner et al. later on investigated the possibility to fine-tune the electrical resistance by co-spraying STF35 with electrically insulating Al$_2$O$_3$.[110] These studies also investigated the annealing behavior of pure STF35 and co-sprayed STF35:Al$_2$O$_3$ composite films. However, to keep a good comparability, we focus on the single-phased films only. The determined DC conductivities of the STF35 film on four-wire gold electrodes are shown in the Arrhenius-like diagram in **Figure 11**. Experiments were conducted in an alumina tube furnace between 300 and 800 °C in air atmosphere. The conductivity σ of the PAD-STF35 film increases from $6 \cdot 10^{-4}$ S cm^{-1} at 300 °C to $3.5 \cdot 10^{-2}$ S cm^{-1} at the highest measured temperature of 800 °C during the initial heating. The almost temperature-independent conductivity with a very low activation energy of $E_a = 0.1$ eV between 700 and 800 °C becomes only apparent on cooling.[133] When the temperature decreases further, σ progressively lowers to $4.9 \cdot 10^{-2}$ S cm^{-1} at 300 °C. As a result, film annealing at $T_{annealing} = 800$ °C increases the total conductivity by a factor of 8.
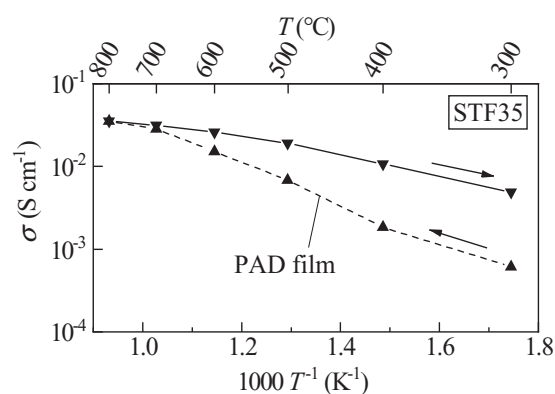

Figure 11. Electronic conductivity of a PAD-STF35 film upon initial heating to 800 °C (▲) and subsequent cooling (▼). Arrows indicate the chronological sequence of the measurements. Adapted with permission.[110] Copyright 2016, Elsevier.

If, instead of STF35, a compound with a higher iron content of 50% (STF50) is used for PAD,[134] the values of the total conductivity are shifted upward by a factor of 2–3; however, the general trend during thermal annealing is identical. In this case, the conductivity increase caused by annealing at 800 °C is slightly higher for STF50 with a factor of 10 compared to 8 for STF35.

Barium Iron Tantalate: BaFe$_{1-x}$Ta$_x$O$_{3-\delta}$ (abbreviated as BFT), just like STF35, is also a semiconducting ceramic material with an oxygen-dependent, yet temperature-independent electronic conductivity.[135] Within the temperature range of 700–900 °C, its electrical conductivity is only affected by the oxygen partial pressure pO_2. Bektas et al. investigated the thermoelectric and electronic properties of BaFe$_{0.78}$Al$_{0.01}$Ta$_{0.20}$O$_{3-\delta}$ (BFAT) of bulk samples and PAD films;[136,137] however, the characteristic annealing behavior of PAD-BFAT films has not been published yet. For this elaboration, however, we were gratefully provided with a corresponding, still unpublished measurement included in his Ph.D. thesis (**Figure 12**).[111]

At 200 °C, the untreated PAD-BFAT film has a conductivity of $\sigma = 1.3 \cdot 10^{-4}$ S cm^{-1}. With rising temperature up to 500 °C, σ increases with a high activation energy of
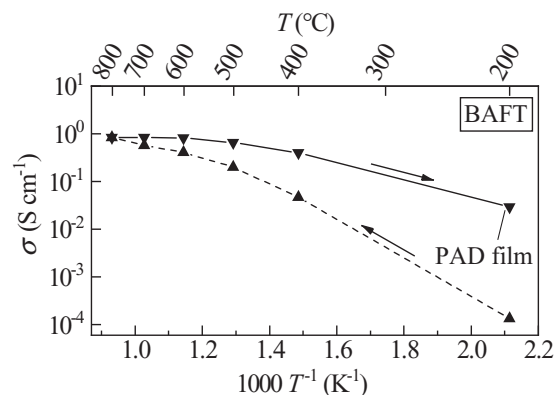

Figure 12. Electronic conductivity of a PAD-BFAT film upon initial heating to 800 °C (▲) and subsequent cooling (▼). Arrows indicate the chronological sequence of the measurements.

E_a = 0.76 eV. Through higher temperatures, films become more conductive up to 0.8 S cm^{-1} at 800 °C, however, at a progressively lowered activation energy that eventually drops to E_a = 0.35 eV at the end of the heating procedure. Only after annealing at $T_{annealing}$ = 800 °C, the temperature-independent conductivity becomes apparent when cooling from 800 to 600 °C. Further cooling to the lowest measured temperature also lowers σ to 3·10^{-2} S cm^{-1}, combined with a progressive incline of E_a to 0.35 eV. While the general annealing behavior of BFAT matches the previous measurements on STF35, where the temperature-independent conductivity is only achieved after an annealing at a temperature $T_{annealing}$ of 800 °C, the absolute change in conductivity values largely differs. For BFAT, the annealing procedure eventually rises the conductivity at the lowest measured temperature by a factor of 220, whereas for STF35 only a relatively small increase by a factor of 8 was observed.

Nickel Manganate: Nickel manganates are spinel type compounds and commonly used in thermistor devices. Their characteristic feature is the negative temperature coefficient of resistance (NTCR),[138] meaning that the electrical resistance decreases exponentially with rising temperatures due to the underlying electron hopping mechanism. Two research groups investigated the powder aerosol deposition of NTCR ceramics with the composition $NiMn_2O_4$. In both preliminary studies, only minor effects of the thermal annealing on the resistance (conductivity) were detected. Observed increases in conductivity by a factor of 6 at 800 °C and 1.7 at 600 °C were reported by Ryu et al. and Schubert et al., respectively.[112,113]

3.1.5. Universal Conductivity Behavior for All PAD Films

For all functional PAD films already published in literature, a post-deposition annealing led to a high electrical conductivity of the films, not depending on the type of the materials' predominant charge carriers. Summarizing all conducted annealing measurements of PAD films, the following conclusion can be drawn:

- Though the electrical conductivity of as-deposited, untreated PAD films is mostly reduced by more than two orders of magnitude, a thermal annealing at a moderate temperature is sufficient to permanently regain the high, near bulk-like electrical conductivity.
- Therefore, a material-dependent, yet characteristic film annealing temperature $T_{annealing}$ could be introduced, that is necessary to recover the materials initial conductivity in PAD films.
- Higher peak temperatures above $T_{annealing}$ do not allow for further permanent improvement of the electrical conductivity.
- Peak temperatures below $T_{annealing}$ may be suitable; however, they result in lower-than-material-intrinsic film conductivities.
- The observed increase in conductivity spreads over a very large range that highly depends on the investigated conductive ceramic material ranging from a minor increase by a factor of 2 for nickel manganates up to four orders of magnitude in case of Li-ion conducting LAGP.

The annealing temperatures that are necessary to regain the maximum conductivities range between relatively low 500 °C for bismuth vanadate and elevated temperatures of 1000 °C (and possibly above) for barium zirconate (BZY20). After the successful annealing procedure is finished, films feature conductivity values close to the corresponding bulk property. In most cases, after annealing, PAD films exhibit only a half or a third of the theoretical conductivity, so the exact bulk values were not reached.

In order to investigate and to understand the effects that are the origin for the deterioration of the electrical properties in the as-deposited state and how the initial material properties are regained through thermal annealing, crystalline and microstructural changes are discussed in the following section on selected examples.

3.2. Microstructural Changes during Thermal Annealing

Three different films are discussed with respect to the crystalline and morphological changes during thermal annealing: bismuth vanadate (BiCuTiVOx) with the lowest annealing temperature of 500 °C, LLZO with a moderate annealing temperature of 600–700 °C and barium zirconate (BZY20) with the highest reported annealing temperature of at least 1000 °C. In the Supporting Information file, SEM images of each used ceramic feedstock powder are shown along with fractured cross-sectional SEM images of produced PAD films in the as-deposited state (Figures S1–S3). Additionally, the particle size distribution of all three feedstock powders are displayed in Figure S4, Supporting Information. The images clearly indicate that the micrometer-sized starting particles consolidate well during PAD while building a nearly dense and well-adhering film. Consequently, the shape of the particles is not apparent any more—instead, a uniform and homogeneous film is visible.

3.2.1. Film Morphology

Exner et al. thermally treated bismuth vanadate films on alumina substrates at temperatures between 200 and 700 °C for 5 h in air and examined the resulting film morphology by SEM.[104] Top view images of the annealed and an untreated as-deposited BiCuTiVOx film are displayed in **Figure 13**.

The image of the untreated films show a characteristic PAD surface. A typical undulation is visible with small craters and hills, formed during randomly impacts of micrometer-sized particles. The RTIC mechanism leads to a flattening of the particles combined with a plastic deformation. For a large number of stochastically impinging particles, this highly consolidated yet irregularly surface forms. There are no micrometer-sized starting particles visible in the image, pointing out that the RTIC mechanism was successful and the untreated BiCuTiVOx film has a pronounced nanocrystalline structure. Films heat-treated at 200 and 300 °C have the same film morphology as untreated films. For films treated at 400–600 °C, some cracks appear, likely related to different thermal expansion coefficients of BiCuTiVOx

**ADVANCED
SCIENCE NEWS**
www.advancedsciencenews.com
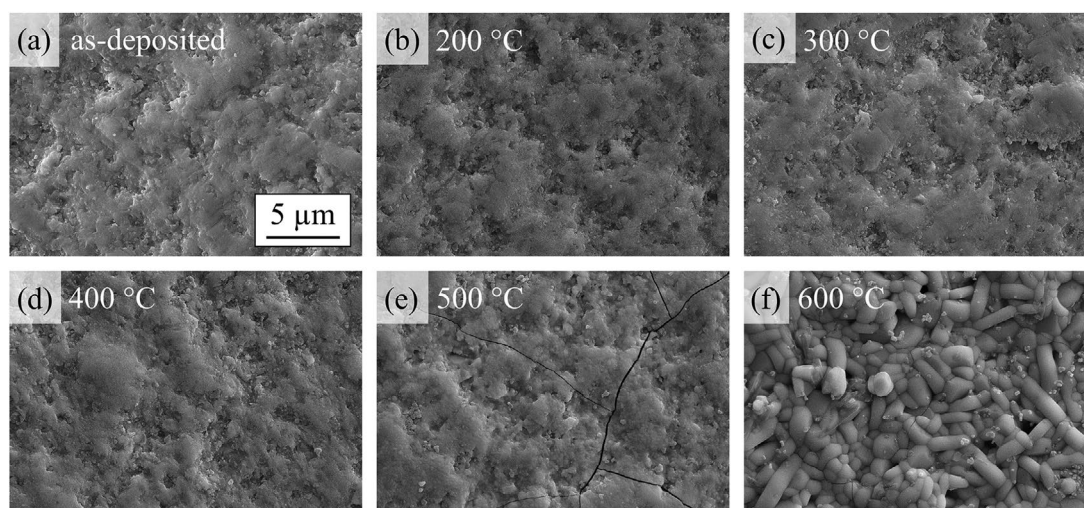
**ADVANCED
MATERIALS**
www.advmat.de

Figure 13. Top view SEM images of PAD-BiCuTiVOx films in the a) as-deposited state and after being thermally annealed at b–f) 200–600 °C. All images use the same scale. Adapted with permission.[104] Copyright 2014, Elsevier.

(14–17 ppm K^{-1})[139] and alumina (5–8 ppm K^{-1}).[140] In addition, a γ–γ' phase transition occurs in BiCuTiVOx at around 440 °C, which is accompanied by a strongly increased coefficient of thermal expansion of up to 25 ppm K^{-1}.[114] However, the film morphologies still match the one of the untreated film. Not until 600 and 700 °C a change in microstructure appears that is caused by markedly growing grains. Sizes of grains increase to 2–3 and 4 μm, respectively. For BiCuTiVOx, an optimum annealing temperature $T_{annealing}$ = 500 °C was determined (see Figure 4), with the majority of the conductivity increase taking place between 300 and 450 °C. Annealing temperatures above 500 °C have no further effect on the electrical conductivity. At first glance, this is an unexpected result, since the temperature range of conductivity increase and film morphology change do not coincide. Therefore, the observed grain growth above 500 °C may not be the reason for the conductivity increase during thermal annealing, at least not for PAD-BiCuTiVOx films.

Similar investigations like for PAD-BiCuTiVOx were conducted for LLZO films by Hanft et al.[108] Top view SEM images of thermally annealed images are displayed in **Figure 14**. The optimum annealing temperature of LLZO was about 600–700 °C. It is of interest, if a change in microstructure occurs for this compound.

The authors found that LLZO films treated at 200 °C also show the typical, nanostructured PAD surface. For the films treated at 300–500 °C, an altered film surface occurs. Sharp crystallites appear at 300 °C and gain in size at 400 and 500 °C. However, at 600 °C these crystallites disappear and a surface that matches the film treated at 200 °C is visible again. This phenomenon is explained through the segregation/formation of a Li$_2$CO$_3$ phase from the volume of the film to the surface.
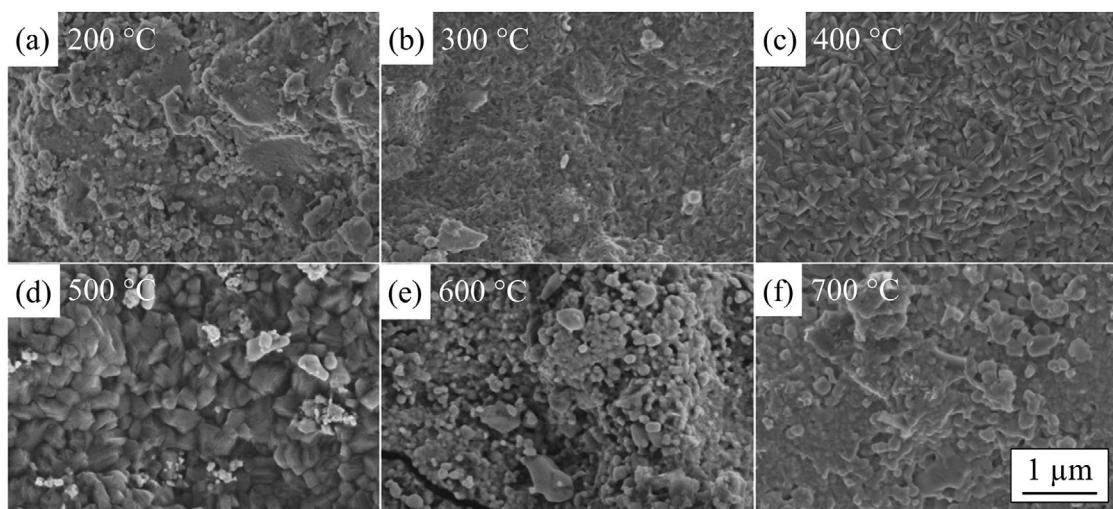

Figure 14. Top view SEM images of a LLZO films after a thermal annealing at a–f) 200–700 °C. All images use the same scale. Adapted with permission.[108] Copyright 2017, Elsevier.
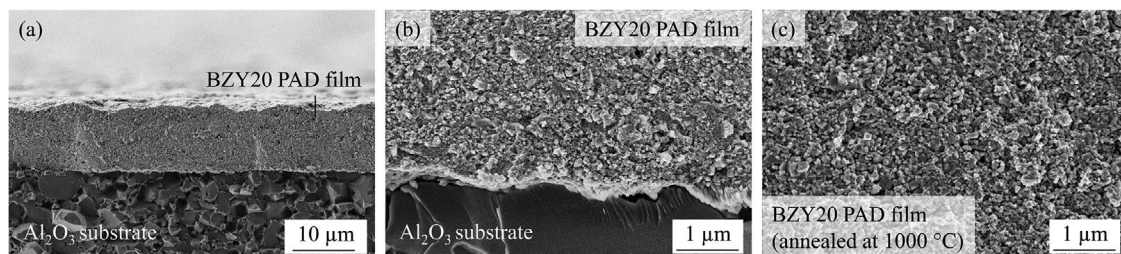
Figure 15. Cross-sectional SEM images of a BZY20 film in the a,b) as-deposited state and c) after a thermal annealing at 1000 °C. Adapted with permission.[106] Copyright 2020, Elsevier.

Lithium carbonate was already present in the starting powder here and was embedded in the LLZO film. After the decomposition of Li_2CO_3 has finished, visible grain growth of LLZO eventually started at temperatures above 600 °C. With the exception of the Li_2CO_3 phenomenon, the evolution of the LLZO microstructure during thermal annealing generally follows the already observed behavior in PAD-BiCuTiVOx films.

The effect of the annealing procedure on the microstructure of a PAD-BZY20 film can be obtained in the SEM images in **Figure 15**. Even though the BZY20 films were treated at a high annealing temperature of 1000 °C, no visible microstructural change is observed, and the film morphology after annealing appears identical to the untreated, as-deposited film. Since this ceramic has a very high melting point of 2600 °C, the chosen annealing temperature is still too low to induce grain growth. Yet, this temperature was already sufficient to permanently increase the ionic conductivity by more than a factor of 700.

From the observation of the coating morphologies, it was hard to identify the clear reason for the drastic change in electrical properties, thus further crystalline analysis was conducted. Consequently, possible changes of the crystalline structure of PAD films during the annealing process were examined.

3.2.2. Crystalline Structure

In order to detect possible changes in the crystallographic material structure during film annealing, X-ray diffraction (XRD) measurements are typically conducted. For a PAD-BiCuTiVOx film on silicon, hot-stage XRD experiments were reported (at room temperature and at 300–800 °C in 50 °C steps).[104] **Figure 16** shows selected XRD patterns of the untreated films at 20 °C and during annealing at 500 °C, as well as of the powder used for powder aerosol deposition.

The BiCuTiVOx starting powder consists mainly of the γ-phase with the tetragonal space group I4/mmm in accordance to ICDD-PDF (International Centre for Diffraction Data–Powder Diffraction File) 01-070-9191.[141] In addition, a small amount of a monoclinic $BiVO_4$ phase (<2 wt%) was detected (marked by "+" in Figure 16). In the untreated BiCuTiVOx film at room temperature, all reflections can be assigned to the γ-phase. Due to the film thickness of 5 μm, sharp reflections from the silicon substrate below the BiCuTiVOx film are also detected (marked by an asterisk). The reflections assigned to the BiCuTiVOx, on the other hand, are markedly broadened, which is caused by the reduced grain size and/or

by the induced microstrain. Both effects may occur during powder aerosol depositing as a result of the underlying RTIC mechanism.[11] On the one hand, particles fracture into fragments with a size of less than 50 nm while impacting onto the substrate, on the other hand, crystalline point and line defects as well as regions with reduced or distorted crystallinity are formed. Due to annealing at increasing temperatures, the width of reflections decreases, as defects are removed and the crystallinity increases. At 500 °C, the BiCuTiVOx coating shows well defined, sharp reflections. Furthermore, slight reflection shifts occur due to the temperature-induced expansion of the unit cell.

The existing XRD patterns from room temperature to 600 °C were examined in detail by Rietveld refinement. This allows for determining both the crystallite sizes and the microstrains (**Figure 17**). The crystallite size in the untreated BiCuTiVOx films is about 30 nm and remains constant up to 350 °C. With a further temperature increase, the crystallite size increases to 35 nm at 400 °C and 95 nm at 500 °C. Due to the strongly deformed and irregular shape of the deposited particles, these values cannot be directly supported by SEM images (Figure 13), but they also do not contradict the previous observations. In the range 500–600 °C, the largest increase in crystallite size occurs to around 2 μm. This observation is in good accordance to the grain growth observed in SEM images of samples being annealed at 600 °C (Figure 13f). The microstrain of the BiCuTiVOx film in the as-deposited state is very high with 0.7% (Figure 17b). Between 300 and 500 °C, it steeply decreases and completely vanishes at 600 °C.
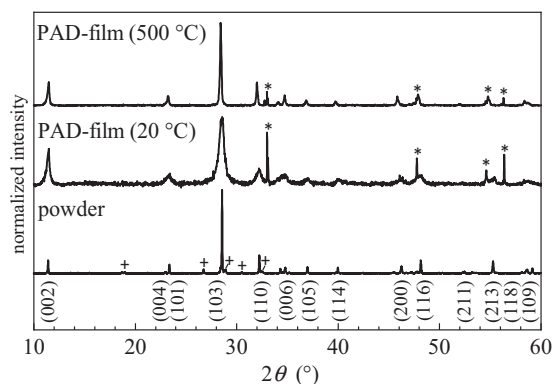

Figure 16. XRD pattern of the BiCuTiVOx powder and the PAD film produced of it in the as-deposited state and after being thermally annealed at 500 °C (silicon substrate). For the meaning of the symbols, see text. Adapted with permission.[104] Copyright 2014, Elsevier.

Combining the thermal film post-treatment results obtained by impedance spectroscopy, scanning electron microscopy, and X-ray diffraction, the behavior of the PAD-BiCuTiVOx film during annealing may be better understood. The powder aerosol deposition leads to a dense, nanocrystalline, and well-adhering film consisting of randomly oriented crystallites of about 30 nm in size. On the crystallographic level, a distinct, stress-induced microstrain of 0.7% is observed. The ionic conductivity of the untreated BiCuTiVOx films is reduced by about two to three orders of magnitude compared to the bulk conductivity. During initial heating of the PAD film, this difference in electrical conductivity to the sintered reference significantly decreases in the temperature range 300–500 °C. This is accompanied by a complete relaxation of the microstrain, while the microstructure (crystallite size and orientation) remains almost unchanged. Further heating eventually leads to the observed grain growth which, however, does not yield a further conductivity increase. This increase in conductivity during the initial annealing is irreversible.

Based on these observations, the significantly reduced ionic conductivity of the untreated BiCuTiVOx films can be directly attributed to the microstrain induced by the RTIC deposition mechanism, which is presumably caused by crystalline point and line defects as well as by amorphization, and thus deteriorates the diffusion pathways of the oxygen ions and lowers their mobility. Furthermore, the deposited nanometer-sized fragments may have a modified valence (e.g., of the V^{5+} cations) at their surroundings, and thus an altered concentration of the oxygen ions. These defects can already be cured by a moderate temperature treatment at 500 °C, far below the sintering temperature of 750–800 °C, whereby the ionic conductivity approaches the bulk conductivity by a factor of 2. Higher temperatures lead to grain growth, but this again does not further improve conductivity.

Similar hot-stage XRD measurements were conducted on cubic LLZO films by Hanft et al.[108] As expected, as-deposited LLZO films exhibited clearly broadened reflections. With increasing annealing temperature, the reflections progressively narrowed as already observed for the PAD-BiCuTiVOx films. Crystallite size and microstrain (**Figure 18**) were derived from the XRD-patterns using Rietveld refinement. For LLZO, highest electrical conductivities (see Figure 10) were achieved after a thermal annealing at between 600 and 700 °C.

In case of PAD-LLZO, the crystallite sizes of the as-deposited films are close to 60 nm. For a thermal annealing up to 500 °C, the crystallite size of the film remains constant. With further heating, the crystallite size increases to 80 and 120 nm at 600 and 700 °C, respectively. On the contrary, the microstrain continuously decreases with increasing annealing temperature from 0.5%
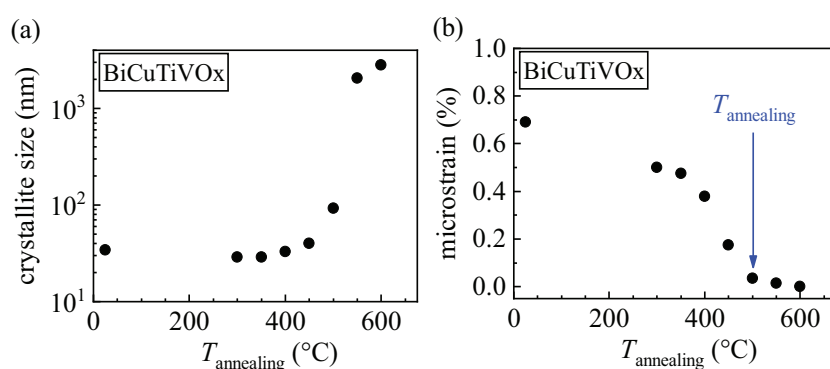

Figure 17. Change of crystalline PAD-BiCuTiVOx film properties during thermal annealing: a) crystallite size and b) microstrain. Adapted with permission.[104] Copyright 2014, Elsevier.

in the untreated state to 0.1% after 600 °C. However, a further reduction or complete relaxation of the microstrain with higher temperatures was not achieved. For LLZO films, as already described for BiCuTiVOx, the necessary annealing temperature $T_{annealing}$ for highest possible conductivities coincides again with the required temperature to minimize the microstrain.

For barium zirconate, the ceramic film with the highest annealing temperature of 1000 °C, a relaxation of the microstrain from 0.3% to below 0.1% was stated as a result of the thermal annealing, yet without any noticeable increase of the crystallite size.[106]

To summarize, the reduction of the microstrain and the underlying restoration of an undistorted crystalline lattice is the key to regain high, near bulk-like electrical conductivities for powder aerosol deposited films. This creates the idea to avoid the formation of microstrain in first place and therefore be able to overcome the necessity of a thermal film post-treatment. However, a successful powder aerosol deposition is always associated with the formation of microstrains, as observed, for example, for ceria films.[64] Well-adhering and consolidated ceria films did only form when particle fracturing with a significant crystallite size reduction according to the RTIC theory occurred, in accordance to observations of Kwon et al. for similar experiments using Y_2O_3 powders.[142,143] However, at the same time, microstrains of 0.5% and higher appeared.[64] Sprayed ceria films with low or even without microstrain only exhibited a minimal mechanical strength without proper consolidation, a state that is often referred to as "chalk-like," and
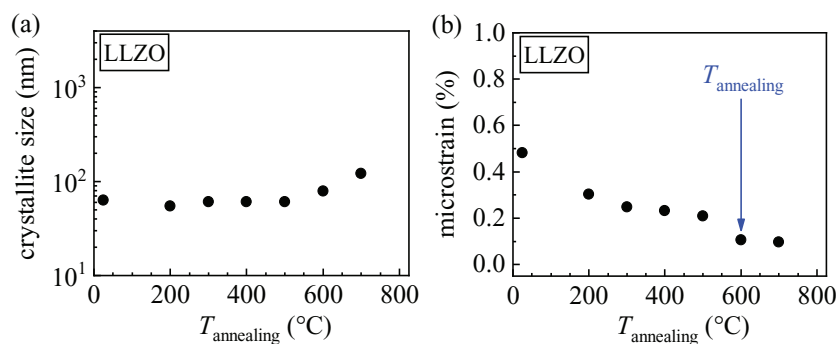

Figure 18. Change of crystalline PAD-LLZO film properties during thermal annealing at $T_{annealing}$: a) crystallite size and b) microstrain. Adapted with permission.[108] Copyright 2017, Elsevier.

Table 2. Coating materials used for powder aerosol deposition, their melting point T_{mp}, as well as the investigated temperature range of thermal post-treatment with the necessary annealing temperature $T_{annealing}$ and the factor of the achieved conductivity increase f_σ.

PAD coating material	Refs.	No.	T_{mp} [°C]	Thermal annealing parameter		
				T-range [°C]	$T_{annealing}$ [°C]	f_σ
BiCuTiVOx	[104]	1	880[144]	200–750	500	72
8YSZ	[105]	2	2700[145]	300–1000	900	39
GDC10	[42]	3	2400[146]	300–1000	800	3
BZY20	[106]	4	2600[147]	400–1000	1000[a]	707
BCY20	[106]	5	1743[148]	300–900	900[a]	65
BSY20	[106]	6	2060[149]	300–1000	900	18
LLZO	[108]	7	1200[150] [b]	200–700	700	237
LAGP	[109]	8	1130[151]	600–750	750	10^4
STF35	[110]	9	2310[152]	300–800	800[a]	8
BFAT	[111][c]	10	1370[153]	200–800	800	222
$NiMn_2O_4$	[112]	11	<1250[154] [b]	600–800	800	6
$NiMn_2O_4$	[113]	12	<1250[154] [b]	200–600	600	1.7

[a] For the three material systems of BZY20 (no. 4), BCY20 (no. 5), and STF35 (no. 9), the end of the annealing process with the full restoration of the initial bulk conductivity has probably not yet been reached, as explained in the corresponding sections; [b] Temperature of decomposition; [c] Data provided by M. Bektas.

therefore appeared like a compacted, highly porous powder agglomerate. Hence, these unconsolidated films are of no use for electrical conducting films. Attempts to reduce the fragmentation and strain formation through a codeposition with a softer component (like PTFE) were successful for dielectric, high-k $BaTiO_3$ films.[88] However, this approach may not be useful for electrical conductors, since charge carrier diffusion will be significantly impeded through the additional, mostly non-conducting phase.

The described behavior results in the dilemma that microstrains and a distorted crystallinity will most likely be present in as-deposited PAD films. Even though the formation of dense functional films is possible at room temperature by RTIC, high and bulk-like electrical conductivities will always require a (thermal) film treatment, at least at the current point of knowledge about PAD. However, understanding the thermal treatment may enable to use the lowest possible annealing temperature. Based on the data of this section, we try to make a prediction of the required annealing temperature $T_{annealing}$ for PAD films.

4. Correlation of Melting Temperature and Annealing Temperature of PAD films

It was shown that for all published conductive functional ceramic films produced by powder aerosol deposition, the electrical conductivity in the as-deposited state is reduced, independent of the predominating conduction mechanism. Through a thermal treatment of the PAD films at temperatures between 500 and 1000 °C, the initially reduced conductivity can be increased. The factor of the maximum conductivity improvement by annealing, abbreviated as f_σ, spreads over a large range from 3 in case of GDC10 to 10^4 for LAGP. Furthermore, the annealing temperature, $T_{annealing}$, above which no further conductivity increase occurs, also depends on the used functional

ceramic. **Table 2** summarizes published PAD films including their investigated temperature range, and the two determined annealing characteristics, f_σ and $T_{annealing}$, and their melting point T_{mp}. For materials without a well-determined melting point, the temperature of thermal decomposition was used instead of T_{mp}.

For most materials in Table 2, the maximum conductivity is also achieved after an annealing at the highest investigated temperature. Thus, it is not certain whether the annealing procedure has already been fully completed or if a further increase in conductivity would be possible at more elevated temperatures. For example, the annealing characteristics of the PAD-$NiMn_2O_4$ films, which were investigated independently by two groups, seem to differ at first glance. Schubert et al. only achieved a slight increase in conductivity of $f_\sigma = 1.7$ at 600 °C, while for Ryu et al. the conductivity increased by $f_\sigma = 5$ at 600 °C and $f_\sigma = 6$ at 800 °C. These deviations could be explained by minor differences in material and/or powder composition or by varying spray parameters. It can therefore be assumed that the crystallite sizes and the microstrains of both untreated films are not identical and that the annealing procedure may therefore have further effects. Additionally, it was also stated by Exner et al., that apparently for compositions with higher doping levels in each material class also larger increases of conductivity f_σ occur.[134] However, this trend has not been understood yet and hopefully can be addressed in future works.

Figure 19 shows the necessary annealing temperature $T_{annealing}$ as a function of the corresponding melting point for functional PAD films already published in literature. Numbering of the 12 points corresponds to Table 2. Both temperature axes use different scaling and suppressed zero points in order to present the data as clearly as possible. This must be taken into account for the interpretation of the displayed data.

There is a clear trend that for increasing melting points T_{mp} also higher annealing temperatures $T_{annealing}$ become necessary, so that the conductivities of the films come close to the bulk
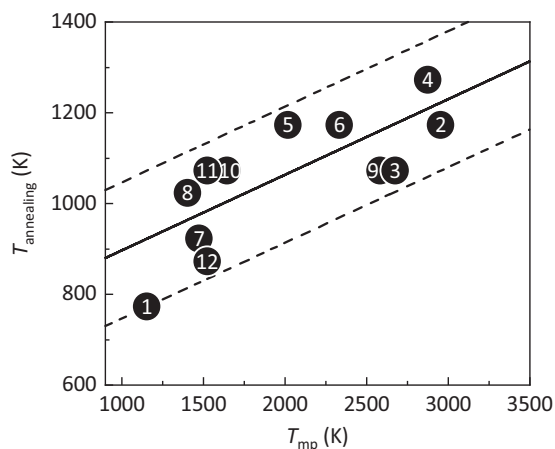
**ADVANCED
SCIENCE NEWS**
www.advancedsciencenews.com

**ADVANCED
MATERIALS**
www.advmat.de

Figure 19. Necessary temperature of thermal annealing $T_{annealing}$ for electrical conductive PAD films as a function of their melting point T_{mp}. Data and numbering according to Table 2: 1 = BiCuTiVOx, 2 = 8YSZ, 3 = GDC10, 4 = BZY20, 5 = BCY20, 6 = BSY20, 7 = LLZO, 8 = LAGP, 9 = STF35, 10 = BFAT, 11 and 12 = NiMn$_2$O$_4$. The black line marks the line of fit according to Equation (1) and dashed lines illustrate a tolerance range of ±150 K.

Figure 20. Relative thermal annealing temperature $T_{annealing}/T_{mp}$ of electrical conductive PAD films as a function of their melting point T_{mp}. Data and numbering according to Table 2: 1 = BiCuTiVOx, 2 = 8YSZ, 3 = GDC10, 4 = BZY20, 5 = BCY20, 6 = BSY20, 7 = LLZO, 8 = LAGP, 9 = STF35, 10 = BFAT, 11 and 12 = NiMn$_2$O$_4$. The black line marks the line of fit according to Equation (1) and dashed lines illustrate a tolerance range of ±150 K.

properties. The low-melting BiCuTiVOx (no. 1) requires the lowest heat treatment, while the high-melting barium zirconate (BZY20, no. 4) does not seem to be completely annealed even after a heat treatment at 1000 °C.

Since $T_{annealing}$ is, in addition to the melting point of the functional ceramic, also affected by the deposition conditions and powder preparation, the data in Figure 19 is not aligned in a single straight line but is scattered over a wider band. Statistical data analysis is carried out using Origin 2018G software. A linear fit function for all 11 measured materials (12 points) leads to the following empirical equation:

$$T_{annealing} = \frac{1}{6} T_{mp} + 730 \text{ K} \tag{1}$$

Equation (1) may be used to predict the necessary annealing temperature $T_{annealing}$ (displayed as the solid line in Figure 19). Please note that all parameters are used in the unit Kelvin. The lower and upper limits of the widened band, marking a temperature offset of ±150 K, are illustrated by dashed lines. The fitted data exhibit values of $R^2 = 0.59$ and $p = 0.004$. A very low p-value smaller $p_{ref} = 0.05$ in generally indicates that changes of the predictor's value (here: $T_{annealing}$) are related to changes of the variable (T_{mp}). This underlines the existence of a significant relationship of both parameters. The R^2 value of 0.6 points out that a medium to large positive linear association exists. However, due to the small number of currently available points combined with possible deviations of $T_{annealing}$ caused by different deposition and powder pretreatment conditions, R^2 is still slightly lowered. Nevertheless, we hope to further refine the dependencies and extend the plot in Figure 19 as more and more annealing data on functional materials will be published.

In all cases, $T_{annealing}$ is well below the melting point T_{mp}. Another important parameter is the relative thermal annealing temperature $T_{annealing}/T_{mp}$. If this parameter is plotted as a function of the melting point T_{mp} (**Figure 20**), it becomes clear that this quotient gradually decreases from around 0.7 at low T_{mp}
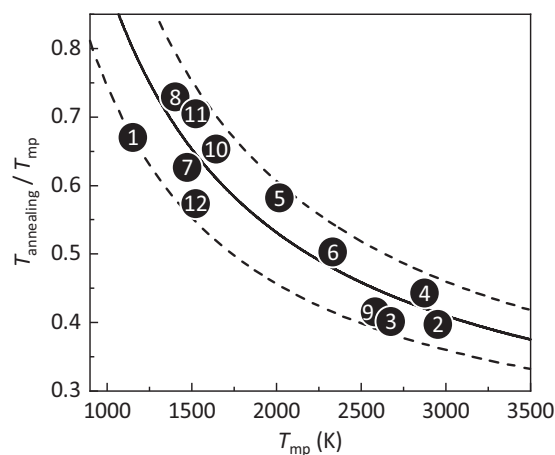
to 0.4 at the highest T_{mp} values. That is particularly beneficial for high-temperature technical ceramics such as 8YSZ (no. 2), GDC10 (no. 3) and BZY20 (no. 4), since this reduces the required annealing temperature.

These findings again underline the assumption that conventional processes such as sintering (grain growth and grain rearrangement) do not play a decisive role in the here-investigated temperature range for annealing of the PAD films. However, the relaxation of the film stress caused by microstrain and the curing of crystalline defects such as dislocations and amorphous lattice regions are dominant. These processes already occur at significantly lower temperatures, far below sintering temperature. Furthermore, PAD films own a large quantity of interfaces between the nanometer-sized crystallites. These boundaries combined with a small amount of nano-porosity may also be important for the annealing behavior of electrically conductive PAD films, since any irregularity of the atomic lattice can act as disturbances and hinder the transport of the electrical charge carriers. Extensive studies using at least high-magnification TEM imaging will be necessary to shed light on this issue; however, they may reveal additional annealing effects that take place at these crystalline interfaces.

The experiments also indicate, that even temperatures lower than the indicated $T_{annealing}$ may be suitable if not the maximum conductivity (of the bulk) is necessary. Besides conventional thermal annealing in a furnace, also a local energy input by high-energy lamps or lasers is under investigation to enhance the functional properties of as-deposited PAD films.[155–157] For dielectric and piezoelectric PAD films, these film properties were already significantly improved by laser annealing.[158–160] Furthermore, it was also proven, that the electrical resistance of PAD-titania films could by tuned by a CW fiber laser.[161]

Even though powder aerosol deposited functional films may currently require a post-deposition treatment to unleash their full potential, their key advantages like the formation of fully dense films with high mechanical stability and substrate adhesion are still unreached by other ceramic deposition techniques.

We also believe that through the ongoing research and development, necessary annealing temperatures $T_{annealing}$ will drop even further and by that make functional PAD films accessible to a large variety of substrate materials and applications.

5. Conclusion

Powder aerosol deposition, to the best of our knowledge, is still the only ceramic coating method that produces dense and well-adhering thick-films directly at room temperature. The only requirements are a suitable ceramic powder and a PAD spray coating apparatus. However, when it comes to functional film properties, these arguments seem oversimplified and things tend to become more and more complex. This brings us back to our initial five questions:

1. Why is a thermal post-treatment of powder aerosol-deposited films necessary at all?

After deposition, mechanical film properties like hardness or plasma resistance as well as the adhesion of the PAD film onto the substrate are remarkably good. However, when it comes to electrical properties like permittivity or electrical conductivity, the nanocrystalline structure of PAD films combined with high internal strains deteriorate most of the characteristic properties. Electrical conductivity is already present within the as-deposited films, yet oftentimes lowered by several orders of magnitude. To regain bulk-like functional properties, a post-deposition treatment is inevitable. Since the treatment is mostly conducted by a thermal annealing procedure, it contradicts PAD's key advantage of full room temperature processing of ceramic films. Understanding the processes taking place during thermal annealing may, however, reduce significantly the required temperatures.

2. Why are functional properties of as-deposited PAD films different than expected?

Since the powder aerosol deposition uses the room temperature impact consolidation mechanism, crystalline defects like dislocations or amorphization in combination with a randomly oriented nanocrystalline microstructure are always present in untreated PAD films. Unfortunately, these microstructure distortions reduce the mobility of all investigated charge carriers.

3. What happens during annealing of PAD films?

The thermal post treatment allows to recover an undistorted crystalline lattice, visible through a decreased or vanished microstrain. Additionally, (nano)-crystallinity increases as previously highly distorted or even amorphous regions rearrange. These processes significantly enhance the electrical conductivity of PAD films, typically over two or more decades. In contrast, grain growth occurs at elevated annealing temperatures, and yet is not believed to be the key driver for the increase of the electrical conductivity.

4. Which temperatures are necessary to achieve the best functional properties?

By joining the already published data on electrical conducting PAD films, a universal annealing behavior was found that leads to a recommendation for the suitable film annealing temperature $T_{annealing}$. The prediction is based on an empirical linear relationship between $T_{annealing}$ and T_{mp}, where T_{mp} is the melting point of the investigated ceramic coating material. This prediction is intended to limit the necessary effort and treatment temperatures. Annealing temperatures range from 500 to 600 °C for low-melting ceramics and from about 1000 to 1100 °C for ceramics with an extraordinary high melting point.

5. Can bulk-like functional properties be regained by thermal annealing?

Thermal annealing of PAD films enables to regain close-to-bulk-like values. After annealing, the conductivities of PAD films slightly fall behind those of conventionally sintered samples by a factor of 2–3. A complete recovery may not be possible due to the still present nanocrystalline film morphology and thus the high number of crystalline interfaces that may act as a barrier for mobile charge carriers.

While, at first glance, any kind of post-treatment seems disadvantageous, temperatures used herein were proven to be far below the ones required for conventional sintering. Therefore, powder aerosol deposition still offers a large potential to form a variety of functional ceramic films for a wide range of applications, especially when dense, high quality films are required.

Supporting Information

Supporting Information is available from the Wiley Online Library or from the author.

Conflict of Interest

The authors declare no conflict of interest.

[1] J. B. Wachtman, R. A. Haber, *Ceramic Films and Coatings*, Noyes Publications, Park Ridge, NJ **1993**.
[2] *Emerging Materials for Energy Conversion and Storage* (Eds: K. Y. Cheong, G. Impellizzeri, M. A. Fraga), Elsevier, Amsterdam **2018**.

**ADVANCED
SCIENCE NEWS**

www.advancedsciencenews.com

**ADVANCED
MATERIALS**

www.advmat.de

[3] K. Lu, *Materials in Energy Conversion, Harvesting, and Storage*, Wiley, New York **2014**.

[4] D. W. Richerson, W. E. Lee, *Modern Ceramic Engineering: Properties, Processing, and Use in Design*, CRC Press, Baton Rouge, LA **2005**.

[5] M. N. Rahaman, *Ceramic Processing*, Chapman and Hall/CRC, Milton, Canada **2017**.

[6] F. Shi, *Ceramic Coatings – Applications in Engineering*, InTech,London **2012**.

[7] K. Choy, *Prog. Mater Sci.* **2003**, *48*, 57.

[8] D. M. Mattox, *Handbook of Physical Vapor Deposition (PVD) Processing*, William Andrew, Oxford **2010**.

[9] R. B. Heimann, *Plasma-Spray Coating*, Wiley-VCH, Hoboken, NJ **2008**.

[10] L. Pawłowski, *The science and Engineering of Thermal Spray Coatings*, Wiley, Chichester, UK **2008**.

[11] D. Hanft, J. Exner, M. Schubert, T. Stöcker, P. Fuierer, R. Moos, *J. Ceram. Sci. Technol.* **2015**, *6*, 147.

[12] J. Akedo, *J. Therm. Spray Technol.* **2008**, *17*, 181.

[13] J.-J. Choi, K.-S. Cho, J.-H. Choi, J. Ryu, B.-D. Hahn, W.-H. Yoon, J.-W. Kim, C.-W. Ahn, J. Yun, D.-S. Park, *J. Eur. Ceram. Soc.* **2012**, *32*, 115.

[14] J.-J. Choi, J.-H. Choi, J. Ryu, B.-D. Hahn, J.-W. Kim, C.-W. Ahn, W.-H. Yoon, D.-S. Park, *J. Eur. Ceram. Soc.* **2012**, *32*, 3249.

[15] J.-H. Jung, B.-D. Hahn, W.-H. Yoon, D.-S. Park, J.-J. Choi, J. Ryu, J.-W. Kim, C.-W. Ahn, K.-M. Song, *J. Eur. Ceram. Soc.* **2012**, *32*, 2451.

[16] M. A. Piechowiak, J. Henon, O. Durand-Panteix, G. Etchegoyen, V. Coudert, P. Marchet, F. Rossignol, *J. Eur. Ceram. Soc.* **2014**, *34*, 1063.

[17] S. Baba, H. Sato, L. Huang, A. Uritani, R. Funahashi, J. Akedo, *J. Alloys Compd.* **2014**, *589*, 56.

[18] M. W. Lee, J. J. Park, D. Y. Kim, S. S. Yoon, H. Y. Kim, D. H. Kim, S. C. James, S. Chandra, T. Coyle, J. H. Ryu, W. H. Yoon, D. S. Park, *J. Aerosol Sci.* **2011**, *42*, 771.

[19] N. H. Khansur, U. Eckstein, L. Benker, U. Deisinger, B. Merle, K. G. Webber, *Ceram. Int.* **2018**, *44*, 16295.

[20] H. Park, J. Kim, C. Lee, *Scr. Mater.* **2015**, *108*, 72.

[21] C.-W. Kim, J.-H. Choi, H.-J. Kim, D.-W. Lee, C.-Y. Hyun, S.-M. Nam, *Ceram. Int.* **2012**, *38*, 5621.

[22] Y. Imanaka, N. Hayashi, M. Takenouchi, J. Akedo, *J. Eur. Ceram. Soc.* **2007**, *27*, 2789.

[23] J. Akedo, I. Masaaki, R. Maeda, *Ferroelectrics* **1999**, *224*, 331.

[24] J. Akedo, M. Lebedev, *Japan. J. Appl. Phys.* **1999**, *38*, 5397.

[25] C. Lee, J. Kim, H. Park, J.-s. Nam, K. S. Son, Y. T. Im, J. W. Lee, B. G. Chung, *J. Met. Mater.* **2016**, *54*, 15.

[26] Y. Wang, X. Suo, C.-J. Li, *Ceram. Int.* **2016**, *42*, 1640.

[27] D.-M. Chun, J.-O. Choi, C. S. Lee, S.-H. Ahn, *Surf. Coat. Technol.* **2012**, *206*, 2125.

[28] J.-H. Park, D.-S. Park, B.-D. Hahn, J.-J. Choi, J. Ryu, S.-Y. Choi, J. Kim, W.-H. Yoon, C. Park, *Ceram. Int.* **2016**, *42*, 3584.

[29] M. Schubert, D. Hanft, T. Nazarenus, J. Exner, M. Schubert, P. Nieke, P. Glosse, N. Leupold, J. Kita, R. Moos, *Funct. Mater. Lett.* **2019**, *12*, 1930005.

[30] E. B. Secor, *Flexible Printed Electron.* **2018**, *3*, 035002.

[31] Y. Cho, J. Hong, H. Ryoo, D. Kim, J. Park, J. Han, *J. Dent. Res. 94*, 491, **2015**.

[32] J.-J. Choi, J.-H. Jang, B.-D. Hahn, D.-S. Park, W.-H. Yoon, J. Ryu, C. Park, *J. Am. Ceram. Soc.* **2007**, *90*, 3389.

[33] J. Ryu, K.-Y. Kim, J.-J. Choi, B.-D. Hahn, W.-H. Yoon, B.-K. Lee, D.-S. Park, C. Park, *J. Am. Ceram. Soc.* **2009**, *92*, 3084.

[34] P. Nieke, J. Kita, M. Häming, R. Moos, *Materials* **2019**, *12*, 487.

[35] T. Miyoshi, *J. Am. Ceram. Soc.* **2008**, *91*, 2098.

[36] M. Lebedev, S. Krumdieck, *Curr. Appl. Phys.* **2008**, *8*, 233.

[37] Y. Imanaka, H. Amada, F. Kumasaka, N. Takahashi, T. Yamasaki, M. Ohfuchi, C. Kaneta, *Adv. Eng. Mater.* **2013**, *15*, 1129.

[38] J.-J. Huang, Y.-P. Fu, J.-Y. Wang, Y.-N. Cheng, S. Lee, J.-C. Hsu, *Mater. Res. Bull.* **2014**, *51*, 63.

[39] S.-Q. Fan, G.-J. Yang, C.-J. Li, G.-J. Liu, C.-X. Li, L.-Z. Zhang, *J. Therm. Spray Technol.* **2006**, *15*, 513.

[40] S. Baba, L. Huang, H. Sato, R. Funahashi, J. Akedo, *J. Phys. Conf. Ser.* **2012**, *379*, 012011.

[41] B.-D. Hahn, Y. Kim, C.-W. Ahn, J.-J. Choi, J. Ryu, J.-W. Kim, W.-H. Yoon, D.-S. Park, S.-Y. Yoon, B. Ma, *Ceram. Int.* **2016**, *42*, 18141.

[42] J. Exner, H. Pöpke, F.-M. Fuchs, J. Kita, R. Moos, *Materials* **2018**, *11*, 2072.

[43] J.-W. Lee, J.-H. Koh, *Sci. Adv. Mater.* **2016**, *8*, 834.

[44] S. D. Johnson, E. R. Glaser, S.-F. Cheng, J. Hite, *Mater. Res. Bull.* **2016**, *76*, 365.

[45] J.-J. Park, J.-G. Lee, D.-Y. Kim, J.-H. Hong, J.-J. Kim, S. Hong, S. S. Yoon, *Environ. Sci. Technol.* **2012**, *46*, 12510.

[46] T. Hoshina, T. Furuta, Y. Kigoshi, S. Hatta, N. Horiuchi, H. Takeda, T. Tsurumi, *Japan. J. Appl. Phys.* **2010**, *49*, 09MC02.

[47] D. Popovici, H. Tsuda, J. Akedo, *J. Appl. Phys.* **2009**, *105*, 061638.

[48] S.-W. Oh, J. Akedo, J.-H. Park, Y. Kawakami, *Japan. J. Appl. Phys.* **2006**, *45*, 7465.

[49] J. Akedo, J.-H. Park, Y. Kawakami, *Japan. J. Appl. Phys.* **2018**, *57*, 07LA02.

[50] R. C. Kambale, D. Patil, J. Ryu, Y. S. Chai, K. H. Kim, W.-H. Yoon, D.-Y. Jeong, D.-S. Park, J.-W. Kim, J.-J. Choi, C.-W. Ahn, *J. Phys. D Appl. Phys.* **2013**, *46*, 092002.

[51] Y. Kawakami, M. Watanabe, K.-I. Arai, S. Sugimoto, *Trans. Mater. Res. Soc. Jpn* **2016**, *41*, 279.

[52] M. Hasegawa, K. Akiyama, Y. Oki, M. Tanaka, S. Kitaoka, Y. Kagawa, *Mater. Trans.* **2016**, *57*, 1714.

[53] H.-J. Kim, S. H. Cho, S. Y. J. Yoon, S.-I. Yoo, *Ceram. Int.* **2015**, *41*, 291.

[54] S. I. Bredikhin, D. A. Agarkov, E. Agarkova, I. Burmistrov, A. Cherkasov, V. Pukha, D. Yalovenko, N. Lyskov, *ECS Trans.* **2019**, *91*, 403.

[55] N. A. Ovsyannikov, G. V. Nechaev, D. V. Novikov, A. A. Bel'mesov, V. E. Pukha, *Russ. J. Electrochem.* **2019**, *55*, 565.

[56] C.-W. Ahn, J.-J. Choi, J. Ryu, B.-D. Hahn, J.-W. Kim, W.-H. Yoon, J.-H. Choi, D.-S. Park, *Carbon* **2015**, *82*, 135.

[57] J. Adamczyk, S. Ghosh, T. L. Braden, C. J. Hogan, E. S. Toberer, *ACS Comb. Sci.* **2019**, *21*, 753.

[58] M. H. Kwak, S. B. Kang, J. H. Kim, J. Lee, S.-M. Lee, W.-J. Kim, S. E. Moon, *J. Ceram. Process. Res.* **2017**, *18*, 731.

[59] K. Sahner, M. Kaspar, R. Moos, *Sens. Actuators B* **2009**, *139*, 394.

[60] D. Hanft, P. Glosse, S. Denneler, T. Berthold, M. Oomen, S. Kauffmann-Weiss, F. Weis, W. Häßler, B. Holzapfel, R. Moos, *Materials* **2018**, *11*, 1572.

[61] S. Kauffmann-Weiss, W. Hässler, E. Guenther, J. Scheiter, S. Denneler, P. Glosse, T. Berthold, M. Oomen, T. Arndt, T. Stöcker, D. Hanft, R. Moos, M. Weiss, F. Weis, B. Holzapfel, *IEEE Trans. Appl. Supercond.* **2017**, *27*, 1.

[62] P. Sarobol, A. C. Hall, D. A. Urrea, M. E. Chandross, J. D. Carroll, B. L. Boyce, W. M. Mook, P. G. Kotula, B. B. McKenzie, D. C. Bufford, *Deformation Behavior of Sub-micron and Micron Sized Alumina Particles in Compression*, Sandia National Laboratories, Albuquerque, NM **2014**.

[63] J. Akedo, *J. Am. Ceram. Soc.* **2006**, *89*, 1834.

[64] J. Exner, M. Schubert, D. Hanft, J. Kita, R. Moos, *J. Eur. Ceram. Soc.* **2019**, *39*, 592.

[65] D.-W. Lee, H.-J. Kim, Y.-H. Kim, Y.-H. Yun, S.-M. Nam, *J. Am. Ceram. Soc.* **2011**, *94*, 3131.

[66] L.-S. Wang, H.-F. Zhou, K.-J. Zhang, Y.-Y. Wang, C.-X. Li, X.-T. Luo, G.-J. Yang, C.-J. Li, *Ceram. Int.* **2017**, *43*, 4390.

[67] M. Schubert, M. Hahn, J. Exner, J. Kita, R. Moos, *Funct. Mater. Lett.* **2017**, *10*, 1750045.

[68] N. H. Khansur, U. Eckstein, Y. Li, D. A. Hall, J. Kaschta, K. G. Webber, *J. Am. Ceram. Soc.* **2019**, *102*, 5763.

[69] K. Naoe, M. Nishiki, K. Sato, *J. Therm. Spray Technol.* **2014**, *23*, 1333.

[70] J. Exner, M. Hahn, M. Schubert, D. Hanft, P. Fuierer, R. Moos, *Adv. Powder Technol.* **2015**, *26*, 1143.

[71] J. Adamczyk, P. Fuierer, *Surf. Coat. Technol.* **2018**, *350*, 542.

[72] M. Schubert, J. Exner, R. Moos, *Materials* **2014**, *7*, 5633.

[73] S. Kim, M.-Y. Cho, I.-S. Kim, W.-J. Kim, S.-H. Park, S. Baek, J.-M. Oh, S.-W. Kim, *Adv. Mater. Interfaces* **2019**, *6*, 1900359.

[74] 2019 Supported Research & Education: Protective Ceramic Coatings by Aerosol Deposition of Extraterrestrial Regolith, New Mexico Space Grant Consortium, http://nmspacegrant.com/2019-supported-research-education/ (accessed: December 2019).

[75] P. Fuierer, R. Calvo, G. Strobel, presented at *Materials Science & Technology (MS&T19)*, Portland, OR, October **2019**.

[76] D.-W. Lee, M.-C. Shin, Y.-N. Kim, J.-M. Oh, *Ceram. Int.* **2017**, *43*, 1044.

[77] Q. Yin, B. Zhu, H. Zeng, *Microstructure, Property and Processing of Functional Ceramics*, Springer, Berlin **2010**.

[78] J. Akedo, M. Ichiki, K. Kikuchi, R. Maeda, *Sens. Actuators A* **1998**, *69*, 106.

[79] M. Lebedev, J. Akedo, *Ferroelectrics* **2002**, *270*, 117.

[80] M. Nakada, K. Ohashi, J. Akedo, *Japan. J. Appl. Phys.* **2005**, *44*, L1088.

[81] M. Iwanami, M. Nakada, H. Tsuda, K. Ohashi, J. Akedo, *IEICE Electron. Express* **2007**, *4*, 26.

[82] J.-H. Park, J. Akedo, M. Lebedev, H. Sato, in *Device and Process Technologies for Microelectronics, MEMS, and Photonics IV* (Eds: J.-C. Chiao, A. S. Dzurak, C. Jagadish, D. V. Thiel), SPIE, Bellingham, WA **2006**, p. 60371S.

[83] H. Palneedi, D. Maurya, G.-Y. Kim, V. Annapureddy, M.-S. Noh, C.-Y. Kang, J.-W. Kim, J.-J. Choi, S.-Y. Choi, S.-Y. Chung, S.-J. L. Kang, S. Priya, J. Ryu, *Adv. Mater.* **2017**, *29*, 1605688.

[84] H. Palneedi, D. Maurya, G.-Y. Kim, S. Priya, S.-J. L. Kang, K.-H. Kim, S.-Y. Choi, J. Ryu, *Appl. Phys. Lett.* **2015**, *107*, 012904.

[85] Y. Imanaka, M. Takenouchi, J. Akedo, *J. Cryst. Growth* **2005**, *275*, e1313.

[86] J.-M. Oh, S.-M. Nam, *J. Ceram. Process. Res.* **2009**, *10*, 674.

[87] J.-M. Oh, S.-M. Nam, *Thin Solid Films* **2010**, *518*, 6531.

[88] Y.-H. Kim, H.-J. Kim, J.-H. Koh, J.-G. Ha, Y.-H. Yun, S.-M. Nam, *Ceram. Int.* **2011**, *37*, 1859.

[89] H.-K. Kim, S.-H. Lee, S. I. Kim, C. Woo Lee, J. Rag Yoon, S.-G. Lee, Y.-H. Lee, *J. Appl. Phys.* **2014**, *115*, 014101.

[90] H. Hatono, T. Ito, K. Iwata, J. Akedo, *Int. J. Appl. Ceram. Technol.* **2006**, *3*, 419.

[91] J. Akedo, M. Lebedev, *Adv. Dielectr. Mater. Electron. Devices* **2006**, *174*, 99.

[92] H.-B. Jung, J.-H. Lim, M. Peddigari, J. Ryu, D. H. Choi, D.-Y. Jeong, *J. Eur. Ceram. Soc.* **2020**, *40*, 63.

[93] D. Damjanovic, *Curr. Opin. Solid State Mater. Sci.* **1998**, *3*, 469.

[94] G. Arlt, D. Hennings, G. de With, *J. Appl. Phys.* **1985**, *58*, 1619.

[95] T. Miyoshi, H. Funakubo, *Japan. J. Appl. Phys.* **2010**, *49*, 09MD13.

[96] T. Hoshina, T. Furuta, T. Yamazaki, H. Takeda, T. Tsurumi, *Japan. J. Appl. Phys.* **2013**, *52*, 09KC05.

[97] T. Kagotani, R. Kobayashi, S. Sugimoto, K. Inomata, K. Okayama, J. Akedo, *J. Magn. Magn. Mater.* **2005**, *290-291*, 1442.

[98] N. H. Khansur, U. Eckstein, K. Riess, A. Martin, J. Drnec, U. Deisinger, K. G. Webber, *Scr. Mater.* **2018**, *157*, 86.

[99] E.-S. Kim, J.-G. Liang, C. Wang, M.-Y. Cho, J.-M. Oh, N.-Y. Kim, *Sci. Rep.* **2019**, *9*, 680.

[100] J. Kim, H. Kwon, H. Park, C. Lee, *Surf. Interfaces* **2017**, *9*, 114.

[101] Y. Yamamoto, Y. Iriyama, S. Muto, *J. Am. Ceram. Soc.* **2020**, *103*, 1454.

[102] T. Moritaka, Y. Yamashita, T. Tojo, R. Inada, Y. Sakurai, *Nanomaterials* **2019**, *9*, 1032.

[103] F. Panzer, D. Hanft, T. P. Gujar, F.-J. Kahle, M. Thelakkat, A. Köhler, R. Moos, *Materials* **2016**, *9*, 277.

[104] J. Exner, P. Fuierer, R. Moos, *Thin Solid Films* **2014**, *573*, 185.

[105] J. Exner, J. Kita, R. Moos, *J. Mater. Sci.* **2019**, *54*, 13619.

[106] J. Exner, T. Nazarenus, J. Kita, R. Moos, *Int. J. Hydrogen Energy* **2020**, https://doi.org/10.1016/j.ijhydene.2020.01.164.

[107] D. Hanft, *Aerosolbasierte Kaltabscheidung Lithium-Ionen leitender Festelektrolytschichten mit Granatstruktur*, Shaker, Düren, Germany **2019**.

[108] D. Hanft, J. Exner, R. Moos, *J. Power Sources* **2017**, *361*, 61.

[109] A. Khan, C.-W. Ahn, J. Ryu, W.-H. Yoon, B.-D. Hahn, J.-J. Choi, J.-W. Kim, D.-S. Park, *Met. Mater. Int.* **2014**, *20*, 399.

[110] J. Exner, M. Schubert, D. Hanft, T. Stöcker, P. Fuierer, R. Moos, *Sens. Actuators B* **2016**, *230*, 427.

[111] M. Bektas, *Ph.D. Thesis*, University of Bayreuth **2020**.

[112] J. Ryu, D.-S. Park, R. Schmidt, *J. Appl. Phys.* **2011**, *109*, 113722.

[113] M. Schubert, C. Münch, S. Schuurman, V. Poulain, J. Kita, R. Moos, *J. Eur. Ceram. Soc.* **2018**, *38*, 613.

[114] P. Fuierer, M. Maier, J. Exner, R. Moos, *J. Eur. Ceram. Soc.* **2014**, *34*, 943.

[115] P. Fuierer, R. Maier, U. Röder-Roith, R. Moos, *J. Mater. Sci.* **2011**, *46*, 5447.

[116] N. Bailly, S. Georges, E. Djurado, *Solid State Ionics* **2012**, *222-223*, 1.

[117] X.-D. Zhou, W. Huebner, I. Kosacki, H. U. Anderson, *J. Am. Ceram. Soc.* **2002**, *85*, 1757.

[118] I. Riess, *Solid State Ionics* **2003**, *157*, 1.

[119] G. Laukaitis, D. Virbukas, *Solid State Ionics* **2013**, *247-248*, 41.

[120] S. Lübke, H.-D. Wiemhöfer, *Solid State Ionics* **1999**, *117*, 229.

[121] G. Taillades, M. Jacquin, Z. Khani, D. Jones, M. Marrony, J. Roziere, *ECS Trans.* **2007**, *7*, 2291.

[122] F. Iguchi, T. Tsurui, N. Sata, Y. Nagao, H. Yugami, *Solid State Ionics* **2009**, *180*, 563.

[123] K. D. Kreuer, St. Adams, W. Münch, A. Fuchs, U. Klock, J. Maier, *Solid State Ionics* **2001**, *145*, 295.

[124] E. Fabbri, D. Pergolesi, S. Licoccia, E. Traversa, *Solid State Ionics* **2010**, *181*, 1043.

[125] A. Braun, S. Duval, P. Ried, J. Embs, F. Juranyi, T. Strässle, U. Stimming, R. Hempelmann, P. Holtappels, T. Graule, *J. Appl. Electrochem.* **2009**, *39*, 471.

[126] J. Tong, D. Clark, L. Bernau, A. Subramaniyan, R. O'Hayre, *Solid State Ionics* **2010**, *181*, 1486.

[127] Y. Wang, A. Chesnaud, E. Bevillon, G. Dezanneau, *Solid State Ionics* **2012**, *214*, 45.

[128] H. Buschmann, S. Berendts, B. Mogwitz, J. Janek, *J. Power Sources* **2012**, *206*, 236.

[129] R. Murugan, V. Thangadurai, W. Weppner, *Angew. Chem., Int. Ed.* **2007**, *46*, 7778.

[130] C. A. Geiger, E. Alekseev, B. Lazic, M. Fisch, T. Armbruster, R. Langner, M. Fechtelkord, N. Kim, T. Pettke, W. Weppner, *Inorg. Chem.* **2011**, *50*, 1089.

[131] R. Moos, W. Menesklou, H.-J. Schreiner, K. H. Härdtl, *Sens. Actuators B* **2000**, *67*, 178.

[132] K. Sahner, R. Moos, N. Izu, W. Shin, N. Murayama, *Sens. Actuators B* **2006**, *113*, 112.

[133] R. Moos, N. Izu, F. Rettig, S. Reiss, W. Shin, I. Matsubara, *Sensors* **2011**, *11*, 3439.

[134] J. Exner, *Aerosolbasierte Kaltabscheidung von Funktionskeramiken für neuartige Anwendungen im Bereich der Sensorik und Energiewandlung*, Shaker, Herzogenrath, Germany **2019**.

[135] M. Bektas, D. Schönauer-Kamin, G. Hagen, A. Mergner, C. Bojer, S. Lippert, W. Milius, J. Breu, R. Moos, *Sens. Actuators B* **2014**, *190*, 208.

[136] M. Bektas, D. Hanft, D. Schönauer-Kamin, T. Stöcker, G. Hagen, R. Moos, *J. Sens. Sens. Syst.* **2014**, *3*, 223.

[137] M. Bektas, T. Stöcker, A. Mergner, G. Hagen, R. Moos, *J. Sens. Sens. Syst.* **2018**, *7*, 289.

[138] A. Feteira, *J. Am. Ceram. Soc.* **2009**, *92*, 967.

[139] A. Yaremchenko, V. Kharton, E. Naumovich, V. Samokhval, *Solid State Ionics* **1998**, *111*, 227.

[140] R. G. Munro, *J. Am. Ceram. Soc.* **1997**, *80*, 1919.

[141] A. A. Yaremchenko, M. Avdeev, V. V. Kharton, A. V. Kovalevsky, E. N. Naumovich, F. M. B. Marques, *Mater. Chem. Phys.* **2003**, *77*, 552.

[142] H. Kwon, Y. Kim, H. Park, C. Lee, *Surf. Coat. Technol.* **2019**, *374*, 493.

[143] H. Kwon, Y. Kim, H. Park, S. Jeong, C. Lee, *Ceram. Int.* **2019**, https://doi.org/10.1016/j.ceramint.2019.12.149.

[144] C. Lee, D. Sinclair, A. West, *Solid State Ionics* **1993**, *62*, 193.

[145] P. L. Fauchais, J. V. R. Heberlein, M. I. Boulos, *Thermal Spray Fundamentals: From Powder to Part*, Springer, Boston, MA **2014**.

[146] Y. Guo, D. Wang, F. Wang, *Opt. Mater.* **2015**, *42*, 390.

[147] S. Duval, P. Holtappels, U. Vogt, E. Pomjakushina, K. Conder, U. Stimming, T. Graule, *Solid State Ionics* **2007**, *178*, 1437.

[148] S. Yamanaka, M. Fujikane, T. Hamaguchi, H. Muta, T. Oyama, T. Matsuda, *J. Alloys Compd.* **2003**, *359*, 109.

[149] Y. H. Ochoa Muñoz, M. Ponce, J. E. Rodríguez Páez, *Powder Technol.* **2015**, *279*, 86.

[150] Y. Zhang, J. Cai, F. Chen, R. Tu, Q. Shen, X. Zhang, L. Zhang, *J. Alloys Compd.* **2015**, *644*, 793.

[151] A. M. Rodrigues, J. L. Narváez-Semanate, A. A. Cabral, A. C. M. Rodrigues, *Mater. Res.* **2013**, *16*, 811.

[152] G. Neri, A. Bonavita, G. Micali, G. Rizzo, R. Licheri, R. Orru, G. Cao, *Sens. Actuators B* **2007**, *126*, 258.

[153] H. J. van Hook, *J. Phys. Chem.* **1964**, *68*, 3786.

[154] G. D. C. Csete de Györgyfalva, I. M. Reaney, *J. Eur. Ceram. Soc.* **2001**, *21*, 2145.

[155] S. Baba, J. Akedo, *J. Am. Ceram. Soc.* **2005**, *88*, 1407.

[156] J. Ryu, presented at *8th Tsukuba Int. Coatings Symp.*, Tsukuba, Japan, December **2018**.

[157] J. Ryu, presented at *13th Pacific Rim Conf. of Ceramic Societies (PACRIM13)*, Okinawa, Japan, October **2019**.

[158] S. Baba, J. Akedo, *Appl. Surf. Sci.* **2009**, *255*, 9791.

[159] S. Baba, J. Akedo, M. Tsukamoto, N. Abe, *J. Am. Ceram. Soc.* **2006**, *89*, 1736.

[160] H. Palneedi, I. Choi, G.-Y. Kim, V. Annapureddy, D. Maurya, S. Priya, J.-W. Kim, K. J. Lee, S.-Y. Choi, S.-Y. Chung, S.-J. L. Kang, J. Ryu, D. Vieland, *J. Am. Ceram. Soc.* **2016**, *99*, 2680.

[161] T. Shinonaga, *J. Laser Micro/Nanoeng.* **2014**, *9*, 204.

1908104 (20 of 20)